Article:
Gómez Martín, JC, Brooke, JSA, Feng, W et al. (2017) Impacts of meteoric sulfur in the Earth's atmosphere. Journal of Geophysical Research: Atmospheres, 122 (14). pp. 7678-7701. ISSN: 2169-897X

https://doi.org/10.1002/2017JD027218

Impacts of meteoric sulfur in the Earth's atmosphere

Juan Carlos Gómez Martín[1*], James S. A. Brooke[1], Wuhu Feng[1,2], Michael Höpfner[3], Michael J. Mills[4] and John M. C. Plane[1*]

[1] *School of Chemistry, University of Leeds, Leeds, UK*

[2] *National Centre for Atmospheric Science, University of Leeds, Leeds, UK*

[3] *Institute of Meteorology and Climate Research, Karlsruhe Institute of Technology, Karlsruhe, Germany*

[4] *Atmospheric Chemistry Observations and Modeling Laboratory, National Center for Atmospheric Research, Boulder, Colorado, USA*

[*] Corresponding Authors (chmjgm@leeds.ac.uk, J.M.C.Plane@leeds.ac.uk)

Key points

- Meteoric sulfur inputs of 1 S t d^{-1} and 3 S t d^{-1} have been incorporated into a chemistry-climate model.
- A meteoric sulfur layer in the MLT is predicted, with high number densities compared to other meteoric elemental constituents.
- The meteoric sulfur flux is focused into the winter polar vortex and contributes to the polar upper stratospheric sulfur budget, including the stratospheric CN layer.

Abstract

A meteoric sulfur input function and a sulfur ion chemistry scheme have been incorporated into a chemistry-climate model, in order to study the speciation of sulfur between the stratosphere and the thermosphere (~20 – 120 km), and the impact of the sulfur input from ablation of cosmic dust. The simulations have been compared to rocket observations of SO^+ between 85 and 110 km, MIPAS observations of SO_2 between 20 and 45 km, and stratospheric balloon-borne measurements of H_2SO_4 vapor and sulfate aerosol. These observations constrain the present day global flux of meteoric sulfur to $\leq$ 1.0 t S d^{-1}, i.e. 2 orders of magnitude smaller than the flux of S into the stratosphere from OCS photo-oxidation and explosive volcanic SO_2 injection. However, the meteoric sulfur flux is strongly focused into the polar vortices by the meridional circulation, and therefore the contribution of SO_2 of meteoric origin to the polar upper stratosphere during winter is substantial (~ 30% at 50 km for a flux of 1.0 t S d^{-1}). The Antarctic spring sulfate aerosol layer is found to be very sensitive to a moderate increase of the input rate of meteoric sulfur, showing a factor of 2 enhancement in total sulfate aerosol number density at 30 km for an input of 3.0 t S d^{-1}. The input rate estimate of 1.0 t S d^{-1} suggests an enrichment of sodium relative to sulfur of 2.7 ± 1.5 and is consistent with a total cosmic dust input rate of 44 t d^{-1}.

1. Introduction

Observations of ion metal layers in the D and E regions by rocket-borne mass spectrometry during the 1960s and 1970s [*Istomin*, 1963; *Narcisi and Bailey*, 1965; *Aikin and Goldberg*, 1973] led to early discussions of the processing of meteoric constituents in the mesosphere-lower thermosphere (MLT) region between 75 and 110 km. The abundance of sulfur in extraterrestrial material is ~2 % wt. in ordinary chondrites (OCs) and 2-6% wt. in carbonaceous chondrites (CCs) [*Kring et al.*, 1996], which attracted some initial interest with regard to meteoric sulfur [*Swider*, 1969]. Putative observation of S^+ in the daytime ionosphere [*Narcisi*, 1969] led to laboratory studies that eventually discarded the existence of this ion in the MLT due to its fast reaction with NO and O_2, suggesting that SO^+ should be the most abundant sulfur-bearing ion [*Fehsenfeld and Ferguson*, 1973]. This was followed by a possible detection of SO^+ by rocket-borne mass spectrometry in 1976 above Wallops Island by NASA payload 18.1006 [*Herrmann et al.*, 1978]. Steady-state calculations indicated that the dominant sulfur-containing species in the MLT should be SO [*Swider et al.*, 1979]. Since the early days of rocket sounding of the upper atmosphere, considerable progress has been made in understanding the chemistry of meteoric metal layers and related phenomena ([*Plane*, 2012; *Plane et al.*, 2015] and references therein). However, due to the marginal evidence of sulfur-bearing ionic species and the complete lack of evidence of neutral species in the MLT, the topic of meteoric sulfur and its atmospheric impact has not received attention for many years.

Biogenic and volcanic emissions of sulfur compounds from the Earth's surface are directly related to the aerosol content of the troposphere and stratosphere, which is a major topic in atmospheric science due to its impact on radiative transfer and ozone depletion [*SPARC*, 2006]. Some studies have deemed the present-day input of meteoric sulfur too low to constitute a significant source of lower atmospheric sulfur [*Turco et al.*, 1981; *Court and*

67 *Sephton*, 2011]. On the other hand, meteoric smoke particles (MSPs), which result from the
68 re-condensation of metal vapors in the upper mesosphere, are believed to impact stratospheric
69 H_2SO_4 and sulfate aerosols (H_2SO_4-H_2O droplets) in a variety of ways [*Turco et al.*, 1981;
70 *Murphy et al.*, 1998; *Mills et al.*, 2005b; *Neely et al.*, 2011; *Plane*, 2012]. The atmospheric
71 ablation of sulfur from interplanetary dust particles (IDPs) has been mostly considered from
72 the point of view of the characterization of the effect of heating on the composition and
73 mineralogy of the particles [*Greshake et al.*, 1998; *Toppani et al.*, 2001; *Taylor et al.*, 2011].
74 Interest in climate change, paleoclimate and the evolution of planetary atmospheres has led to
75 a few recent studies of the conditions under which an extra-terrestrial source of sulfur could
76 be climatically relevant, either from meteorite impacts [*Kring et al.*, 1996] or from ablation of
77 IDPs [*Court and Sephton*, 2011], although the connection to metal layers and MSPs and a
78 global atmospheric treatment have not been considered.

79 There are several motivations to revisit the topic of meteoric sulfur and its atmospheric
80 impact. First, a better understanding of the relevant sulfur neutral and ion chemical and
81 photochemical processes now exists than when modeling of the meteoric sulfur layer was
82 first attempted [*Swider et al.*, 1979]. Second, sophisticated chemistry-climate global models
83 are available, where MLT neutral and ion chemistry and calibrated meteoric input functions
84 (MIFs) for different metals can readily be implemented, and transport and other relevant
85 processes are accounted for [*Feng et al.*, 2013; *Marsh et al.*, 2013a; *Plane et al.*, 2016].
86 Third, estimates of the yield of sulfur from flash heating studies of IDP analogues under
87 atmospherically relevant conditions have been reported [*Greshake et al.*, 1998; *Court and*
88 *Sephton*, 2011; 2014]. And fourth, zonally-averaged, vertically-resolved observations of SO_2
89 up to 45 km altitude obtained with the Michelson Interferometer for Passive Atmospheric
90 Sounding (MIPAS) instrument have been published recently [*Höpfner et al.*, 2013], which

helps to constrain the extra-terrestrial flux against the background dominated by surface emissions.

In this paper we describe a study of the global distribution of meteoric sulfur in the Earth's middle atmosphere using the Community Earth System Model - version 1- with the Whole Atmosphere Community Climate Model (CESM1-WACCM) [*Marsh et al.*, 2013b], into which is added an updated sulfur ion chemistry scheme and a sulfur MIF. We discuss the major neutral and ionic carriers of sulfur, and investigate the flux of these into the upper stratosphere and compare it to the flux from below.

2. Model description

CESM1-WACCM is a "high-top" coupled chemistry-climate model with an upper boundary at 6.0×10^{-6} hPa (~140 km). It uses 88 levels (with specified dynamics) from the surface to ~140 km with a spacing ~1.75 km in the stratosphere increasing to ~3.5 km in the thermosphere. The standard horizontal resolution is 1.9° × 2.5° (latitude × longitude). CESM1-WACCM includes diurnal tides and lower *E* region ion chemistry, and contains parameterizations for key MLT phenomena such as the solar cycle and energetic particle precipitation [*Marsh et al.*, 2007]. The model uses specified dynamics where the dynamical fields in the troposphere and stratosphere are nudged to the Modern-Era Retrospective Analysis for Research and Applications (MERRA) meteorological dataset [*Rienecker, Michele M. et al.*, 2011].

We run CESM1-WACCM with sulfur chemistry [*Campbell et al.*, 2014] coupled to a particle microphysics model, the Community Aerosol and Radiation Model for Atmospheres (CARMA) [*Toon et al.*, 1988], to simulate stratospheric sulfate aerosol (SSA). CARMA handles aerosol nucleation, growth, evaporation, coagulation, and sedimentation. Only pure sulfate aerosol (i.e. aerosol composed of H_2SO_4 and H_2O) is considered; the model does not

simulate MSPs (see e.g. [*Brühl et al.*, 2015]), and so nucleation of sulfate aerosol by these particles is neglected. The potential consequences of doing this when evaluating the impact of meteoric sulfur are discussed below. In CARMA, sulfate aerosols are divided into 30 size bins with sulfate mass increasing by a factor of 2.4 between adjacent bins. The dry radii of these size bins range from 0.343 nm to 1.63 μm. CESM1-WACCM outputs a weight % of sulfate in sulfate-water aerosol according to thermodynamic equilibrium, from which wet radii are calculated offline.

2.1. Mesospheric sulfur chemistry

The atmospheric cycle of sulfur is depicted in **Figure 1**, where the precursor species are highlighted. Carbonyl sulfide (OCS) is specified with a constant volume mixing ratio (VMR) at the surface of 510 pptv. Dimethyl sulfide (DMS) oceanic emissions are implemented as described by Lamarque et al. [2012]. SO_2 surface emissions are from a two-dimensional monthly mean surface emissions dataset [*Lamarque et al.*, 2010; *Smith, S J et al.*, 2011]. SO_2 injection from volcanic eruptions follows the new inventory by *Mills et al.* [2016]. The MIF of atomic sulfur is described in section 2.2. The sulfur neutral chemistry in CESM1-WACCM considers eight gas-phase species (S, SO, SO_2, SO_3, $HOSO_2$, H_2SO_4, OCS and DMS) and 22 chemical and photolysis reactions [*English et al.*, 2011].

The most recent implementation of sulfur photochemistry [*Mills et al.*, 2016] is used. Photolysis of H_2SO_4 by visible light is thought to play an important role in sulfur partitioning above 30 km [*Vaida et al.*, 2003], and therefore photolysis cross sections for the v = 4, 5 and 6 OH stretching overtones of H_2SO_4 have been included. These incorporate experimental absorption cross sections [*Feierabend et al.*, 2006] and theoretical pressure-dependent quantum yields [*Miller et al.*, 2007], which account for band-dependent quenching of vibrationally excited states. Near-infrared photolysis at v=3 (966 nm) is not considered, since it falls below the dissociation threshold, which we estimate to be at 777 nm (155 kJ mol^{-1})

from quantum chemistry calculations carried out with the GAUSSIAN 09 software [*Frisch et al.*, 2009] at the accurate W1U level of theory [*Parthiban and Martin*, 2001]. The calculation of H_2SO_4 photolysis rates also includes photolysis by Lyman-α [*Lane and Kjaergaard*, 2008], which is important above 60 km.

In this study we have added reactions between neutral and ionic sulfur species and the major atmospheric ions and molecules listed in **Table 1**. The rate constants in the Table are taken from a compilation of ion-molecule reaction kinetics data [*Anicich*, 2003], and from a review of dissociative recombination rate constants [*Florescu-Mitchell and Mitchell*, 2006]. Wherever data for one reaction is not available, the rate constant of an analogous reaction has been adopted, as indicated in Table 1. For those reactions for which no data was available, dipole-ion capture rate constants were calculated [*Georgievskii and Klippenstein*, 2005]. The major source of S-bearing ions is the charge transfer reaction of SO with O_2^+ (R4). Charge exchange reactions of S atoms (R1, R2 and R3) can be neglected due to the rapid reaction of S with O_2 ($k = 2.3 \times 10^{-12}$ cm^3 molecule^{-1} s^{-1} [*Sander et al.*, 2011]). In contrast to most meteoric components, charge transfer between SO and NO^+ (a major ion in the lower *E* region, usually more abundant than O_2^+) is endothermic (R14). Charge transfer between SO and SO_2 and N_2^+ (R5 and R6) are negligible sources of sulfur ions below 120 km and may have only minor impact above 120 km in high-lying sporadic E layers. Photo-ionization (PI) of S ($J \sim 3 \times 10^{-6}$ s^{-1} [*Swider*, 1969]) is much slower than reaction with O_2^+. PI of SO ($J \sim 10^{-7}$ s^{-1}, see **Fig. S1** in the Supplementary Material) is two orders of magnitude slower than charge transfer with O_2^+. Therefore, PI of S and SO has been omitted from the model.

The major loss process of sulfur-bearing ions is the dissociative recombination of electrons with SO^+ (R15). The fast reaction of S^+ with O_2 (R7) [*Fehsenfeld and Ferguson*, 1973] rapidly converts S^+ into SO^+, which then is removed by electrons. Note that, in contrast to sulfur, for most meteoric metals the reactions analogous to R7 are endothermic, and therefore

the reaction of the oxide cation with abundant O atoms reforms the bare metal cation and competes effectively with neutralization by dissociative recombination (DR) with electrons [*Plane et al.*, 2015]. Reactions of SO^+ and SO_2^+ with other minor atmospheric constituents also promote neutralization. A fast photolysis rate of SO^+ is unlikely considering its high photo-dissociation threshold (225 nm), which constrains photolysis to the VUV, and the significantly different equilibrium distance of the ground state and the high lying accessible excited states, which probably results in small transition probabilities [*Ben Houria et al.*, 2006].

2.2 Meteor input function

Measurements of sulfur-containing species in the MLT are restricted to a handful of mass spectrometric observations of SO^+ (see below). Therefore, the development of a sulfur MIF must necessarily be based on scaling the MIF of a well-studied meteoric elemental constituent such as sodium [*Gardner et al.*, 2014; *Gardner et al.*, 2016]. Scaling to a sodium MIF requires knowledge of the relative abundance of sulfur with respect to sodium in the incoming flux of IDPs, and the relative ablation efficiencies of sulfur and sodium.

Depletions of sulfur and sodium have been reported for most micrometeorites (MMs) and stratospheric IDPs [*Jessberger et al.*, 2001]. There is evidence that this depletion results to a large extent from evaporation during atmospheric entry [*Brownlee*, 1996; *Thomas et al.*, 1996; *Greshake et al.*, 1998; *Toppani et al.*, 2001; *Taylor et al.*, 2011; *Gómez Martín et al.*, 2017]. The pre-entry sulfur and sodium content of IDPs can be deduced from well-known abundances in different groups of meteorites, provided that a link between these and IDPs can be established. The sulfur and sodium contents by weight are respectively 2% and 0.65% in OC meteorites; ~6% and 0.49% in CC meteorites of CI type; and ~3% and 0.41% in CC meteorites of CM types [*Hutchison*, 2004]. A study of MMs collected in the South Pole

189 Water Well (SPWW) at the Scott–Amundsen base in Antarctica [*Taylor et al.*, 2012]
190 indicates that ~75% are fine grained aggregates with CI or CM composition, with less than
191 ~10% corresponding to ordinary chondritic material and ~15% to coarse-grained anhydrous
192 minerals. The sulfur and sodium contents of these meteoritic groups [*Hutchison*, 2004] and in
193 coarse stratospheric IDPs [*Schramm et al.*, 1989], weighted with the aforementioned SPWW
194 group abundances, results in on average 4.12% wt. of sulfur and 0.47 % wt. of sodium in the
195 incoming mass of IDPs (**Table 2**). Thus, the S to Na abundance ratio in IDPs is estimated to
196 be m_S/m_{Na} = 8.8 in terms of mass mixing ratios and x_S/x_{Na} = 6.3 in terms of molar mixing
197 ratios.

198 Large fractions of sulfur have been observed to evaporate from IDP meteoritic analogues at
199 relatively low temperatures (1000-1500 K) in laboratory heating experiments [*Klöck et al.*,
200 1994; *Greshake et al.*, 1996; *Toppani et al.*, 2001]. For instance, heating samples of the CI
201 meteorite Orgueil at 1500 K and under a few microbar of O_2 (relevant for the MLT) resulted
202 in the release of ~90% of the sulfur content after 10 s [*Toppani et al.*, 2001]. However, the
203 general problem of this type of laboratory study is the application of heating curves that
204 neither resemble realistic entry heating profiles, nor reflect the dependence of heating profiles
205 on IDP mass and size. An estimate of the ablation efficiency of sulfur will be derived in the
206 future from the Meteor Ablation Simulator [*Bones et al.*, 2016], as done recently for sodium
207 and iron [*Gómez Martín et al.*, 2017]. A tentative solution is adopted here by comparing the
208 abundances of sulfur and sodium in stratospheric IDPs [*Schramm et al.*, 1989; *Arndt et al.*,
209 1996] and MMs [*Kurat et al.*, 1994; *Genge et al.*, 1997]. The average S/Na ratio in IDPs and
210 MMs (Fig. S2) is within 35% of the S/Na ratio of 6.5 deduced above (within a factor of 2
211 considering the scatter of the measured abundances), which would indicate that the ablation
212 efficiency of both elements is similar. Sulfur could be expected in principle to ablate more
213 efficiently by looking at the large yields from heated meteorite samples observed even at

temperatures lower than the Fe-FeS eutectic (1261 K) [*Burgess et al.*, 1991; *Greshake et al.*, 1998], compared to the small loss of sodium from meteoritic samples heated up to the sodic feldspar melting temperature of ~1400 K [*Jurewicz et al.*, 1993].

To estimate the input rate of meteoric sulfur, we use a recently published determination of the sodium input rate of (2.0 ± 0.4) $\times 10^4$ Na atoms cm^2 s^{-1} (0.34 ± 0.07 t Na d^{-1}) [*Gardner et al.*, 2014; *Gardner et al.*, 2016]. This has to be multiplied by the relative atomic abundance of S/Na in IDPs $(\delta/\gamma)\times(x_S/x_{Na})$, where δ and γ are enrichment or depletion factors with respect to the weighted chondritic abundance derived above (**Table 2**), and by the ablated fraction of sulfur relative to the ablated fraction of sodium (ϕ_S/ϕ_{Na}):

$$MIF_S = MIF_{Na} \times \frac{\delta\, x_S}{\gamma\, x_{Na}} \times \frac{\phi_S}{\phi_{Na}} \qquad \text{(E1)}$$

In this expression we have set δ/γ = 1 and x_S/x_{Na} = 6.3, and we have tentatively assumed ϕ_S/ϕ_{Na} =1. This results in a sulfur input rate of 1.24 × 10^5 atoms cm^{-2} s^{-1} (3.0 t S d^{-1}). Finally, a MIF can be constructed by scaling to this total input rate the relative meteoric input derived from radar observations [*Feng et al.*, 2013; *Marsh et al.*, 2013a], which accounts for the seasonal dependence and the injection altitude. Note that the sodium input flux used by Marsh et al. [2013a] to reproduce the Na layer observations is a factor of ~ 10 smaller than that derived from observations [*Gardner et al.*, 2014; *Gardner et al.*, 2016]. This appears to be due to the vertical transport of Na species being underestimated: CESM1-WACCM does not resolve gravity waves with wavelengths smaller than the horizontal grid scale of ~ 150 km, and thus does not resolve dynamical transport due to dissipating gravity waves, or chemical transport which can be significant when a species is converted to a long-lived reservoir or sink via a pressure-dependent recombination reaction [*Gardner et al.*, 2016]. As a consequence, using the measured input of Na or Fe in the model results in an

237 overestimation of these species in the MLT because they are not flushed downwards quickly
238 enough. This effect is, however, not expected in the case of sulfur, because the chemistry
239 involved is linear in S and the only sink in the MLT is transport by the meridional circulation
240 towards the winter pole and downwards. Moreover, the full impact of the meteoric sulfur
241 input on lower atmospheric layers can only be gauged by implementing a realistic S-MIF in
242 the model. Therefore, we scale the measured sodium flux by the sulfur relative abundance.

243 The assumed MIF injects atomic sulfur between 90 and 125 km, with the peak injection rate
244 at 105 km. Although in some laboratory experiments evaporation of SO_2 has been reported
245 [*Court and Sephton*, 2011; 2014], during atmospheric entry dissociation of molecular species
246 would immediately follow as a result of hyperthermal collisions with air molecules. Part of
247 the evaporated sulfur will also be ionized by collisions [*Vondrak et al.*, 2008], although much
248 less efficiently than Na due to the higher ionization potential of S. In any case, the ions
249 generated during entry will be quenched to their steady state concentrations by chemistry
250 within a short period of time.

251 **2.3. Simulations**

252 Three model simulations for the period 2002 – 2012 were run using the specified dynamics
253 version of CESM1-WACCM, with meteorological values nudged below 50 km using the
254 Modern-Era Retrospective Analysis for Research and Applications (MERRA) reanalysis
255 [*Rienecker, M. M. et al.*, 2011]. This is the period during which MIPAS carried out SO_2
256 measurements up to 45 km altitude [*Höpfner et al.*, 2013]. The first model run includes
257 neutral and ion reactions but no meteoric input (termed the *reference* simulation), and the
258 second run considers the sulfur MIF with the S-MIF = 6.3 × Na-MIF (termed the *S-MIF*
259 simulation). A further simulation was then carried out with a 3-fold reduction of the meteoric
260 sulfur input, i.e. S-MIF = 2.1 × Na-MIF (termed the *S-MIF/3* simulation), in order to test the

dependence of the abundances of meteoric sulfur-bearing species on the sulfur injection rate. Sulfur ion chemistry is considered a previously missing part of the WACCM chemistry module and was therefore included in the reference run. Preliminary runs with the standard CESM1-WACCM neutral S chemistry [*English et al.*, 2011; *Campbell et al.*, 2014] demonstrated that ion chemistry is only relevant in the MLT, as expected.

3. Results

The results obtained when CESM1-WACCM is run without ion chemistry and ablation are in agreement with the previous state-of-the-art modeling study of sulfur using CESM1-WACCM [*Mills et al.*, 2016]. Including sulfur ion chemistry in the model results in negligible changes in the lower atmosphere, since ionic species can only form in the MLT where, in the absence of ablated sulfur, very small concentrations would be present. **Figure 2*a*** shows globally and annually averaged number density profiles of the major sulfur species considered in the model. Three important results illustrated in **Figure 2*a*** are: first, that the total sulfur number density in the MLT, the lower mesosphere and the upper stratosphere is significantly larger when the injection of meteoric sulfur is included; second, that the only significant ionic species SO^+ is very minor compared to the major neutral species; and third, that SO is the dominant species in the MLT, and SO_2 in the middle mesosphere. The largest enhancement from meteoric ablation occurs in the MLT, where the difference with respect to the reference model run increases from ~1 order of magnitude at 80 km to 2 orders of magnitude at 100 km for the S-MIF run. Meteoric sulfur forms a strong SO layer peaking at ~92 km and a weak SO^+ layer peaking at 98 km. SO_2 overtakes SO at 88 km and is the form in which sulfur is transported down to the lower atmospheric layers, where there is an increasingly large contribution of sulfur from the surface. **Figure 2*b*** shows that meteoric and surface total sulfur balance around 62 km in the S-MIF run (the grey line shows the global

285 average of the contribution of meteoric sulfur to the total). Globally, meteoric sulfur remains
286 a significant contribution down to 30 km. **Figure 2*c*** shows that the reduction of the meteoric
287 input by a factor of 3 results in an average reduction of gas phase sulfur by the same factor,
288 although in the mesosphere and below there are significant differences with latitude.

289 **3.1. The meteoric SO layer in the MLT and enhanced mesospheric SO_2.**

290 SO^+ (**Figure 3,** left column) is the major sulfur ionic species, showing a peak around 98 km
291 at mid-latitudes of the order of 50 ions cm^{-3}. In the model sulfur is injected in neutral atomic
292 form as discused above. However, the concentration of S is very small in the MLT due to its
293 rapid reaction with O_2 and only increases with altitude towards the thermosphere. SO (**Figure**
294 **3,** middle column) is the most abundant sulfur-bearing species in the MLT, with a peak of
295 ~1.5×10^5 molecules cm^{-3} at ~ 92 km. SO and SO^+ are coupled by reactions with weak
296 temperature dependences (R4 and R15), which leads to very similar seasonal and latitudinal
297 distribution of these species. The SO^+ layer peaks 8 km higher than the SO layer, following
298 the O_2^+ vertical profile. SO and SO^+ VMRs show similar seasonal variability, but peak at
299 high latitudes and between 100 and 120 km altitude (**Figure S3**). This altitude range is where
300 the MIF peaks. The altitude difference between the peak VMR and number density highlights
301 the rapid transport of sulfur downwards following ablation. The highest mixing ratios (ppbv
302 levels) of sulfur species anywhere above 10 km are reached in the MLT when meteoric sulfur
303 ablation is included in the model.

304 SO_2 (**Figure 3,** right column) is the second species in importance after SO in the MLT. SO
305 and SO_2 are coupled by SO_2 photolysis and the temperature-dependent SO + O_2 reaction. SO
306 peaks at mid-latitudes in summer, but the mid-latitude southern hemispheric SO maximum is
307 a permanent feature of the SO layer that creates a hemispheric asymmetry. SO_2 maximizes at
308 high latitudes in the winter hemisphere at the expense of SO. This leads to the downward

transport of meteoric sulfur in the form of SO_2, whose enhanced concentrations expand over a much wider range of altitudes into the mesosphere (**Figure 4**). Generally, transport in the upper mesosphere is upwards near the summer pole, globally from the summer to winter pole, and downward near the winter pole. Thus, meteoric sulfur is strongly focused towards high latitudes [*Gabrielli et al.*, 2004; *Bardeen et al.*, 2008; *Megner et al.*, 2008; *Hervig et al.*, 2009], and has a very small effect on SO_2 concentrations in the lower tropical mesosphere. Enhanced SO_2 VMRs are localized at high latitude in winter and cover a wide altitude range from 120 to 80 km, which shows how meteoric sulfur is transported downwards by air masses descending within the polar vortices (**Figure S3**). The double peak of the SO_2 VMR in the MLT results from the temperature dependence of the SO + O_2 reaction, so that the reaction is slowest around the local temperature minimum at the mesopause.

The S-MIF/3 simulation generates almost identical layers in the MLT, but with number densities smaller by a factor of 3. As shown in **Figure 2*c***, the gas-phase sulfur abundance remains proportional to the sulfur input flux in the MLT, which as discussed above results from the absence of permanent sinks.

3.2 Meteoric sulfur in the upper and middle stratosphere

Figure 5 shows the stratospheric seasonal averages of SO_2 from the reference run (black contour lines) overlaid with the SO_2 change relative to the S-MIF and S-MIF/3 simulations (left and right columns, respectively). As in the mesosphere, meteoric sulfur increases the SO_2 mixing ratios at high latitudes, particularly in the winter hemisphere. The changes in equatorial and mid-latitudes are small, but in the winter southern hemisphere enhancement of SO_2 is significant above the altitude range where polar stratospheric clouds form. It is well known [*Mills et al.*, 2005b] that, at the onset of spring, the SO_2 transported down the polar vortex during winter is oxidized to SO_3 by OH formed from H_2O photolysis; this results in

higher levels of SO_3, plotted as black contours in **Figure 6**, bottom panel row. SO_3 subsequently associates with H_2O to form H_2SO_4 (black contours in **Figure 7**, bottom panel row). In the S-MIF run, meteoric sulfur significantly contributes to springtime H_2SO_4 formation in both hemispheres, as demonstrated by the relative change colored contour plots in **Figure 6** and **Figure 7**. Changes in SO_3 and H_2SO_4 are most significant at those altitudes and latitudes where the reference simulation levels are higher, i.e. in the 30 - 40 km altitude range and above 70° latitude. Notably, H_2SO_4 increases by more than 20% at 30 km and 75°S. In the S-MIF/3 simulation the distribution of H_2SO_4 is similar, but the enhancements fall below 10% in the aforementioned sensitive regions.

Pure sulfate condensation nuclei (CN) are also affected by meteoric sulfur, which increases their number densities and the pure sulfate surface area density (SAD). The seasonally averaged number densities for the first CN bin and for the sum of the bins with wet radii larger than 3 nm are contour-plotted in **Figure 8** for the reference simulation. The polar spring production of H_2SO_4 results in binary nucleation of H_2SO_4 and H_2O, forming SSA by coagulation and condensation - known as the polar stratospheric CN layer. A meteoric input of 3 t S d^{-1} has a significant impact on the first CN bin (**Figure 8**, left column, second and fourth panels). The largest increases (more than 100%) occur at altitudes higher than 35 km where the CN number density is lower than 1 cm^{-3} (the region with densities lower than 1 cm^{-3} are screened for clarity). The relevant increases in number density are confined to the polar regions during spring, particularly in the southern hemisphere. CN with radii larger than 3 nm only experience enhancement by meteoric sulfur in the Antarctic spring between 25 and 30 km altitude, with a peak change of 70%. The total sulfate CN number density (**Figure 9**, left column) mainly reflects the large increase in the first CN size bin. Regarding sulfate CN surface area density, the S-MIF simulation shows increases of 80% at 30 km and 40% at 25 km in the southern hemisphere at 75°S (**Figure 9**, right column). In the S-MIF/3 run (**Figure**

S4 and **S5**) the enhancements in CN number densities with respect to the reference run are approximately half those in the S-MIF run.

3.3. Comparison with observations

A comparison of the averaged rocket measurements of mass to charge ratio (m/z) = 48, from day-time and twilight (i.e. solar zenith angle < 96°) flights, with modeled vertical profiles of SO^+ is shown in **Figure 10**. Two of these rockets were launched from Wallops Islands (37.8° N, USA) on 12/Aug/1976 11:58 LT (payload 18.1006 [*Meister et al.*, 1978]) and 01/Jan/1977 14:03 LT (payload 18.1008 [*Meister et al.*, 1978]). Four more were launched from Kiruna (67.8° N, Sweden) on 30/Jul/1978 01:32 LT (payload S26/1 [*Kopp et al.*, 1985b]), 13/Aug/1978 01:38 LT (payload S26/2 [*Kopp et al.*, 1985b]), 16/Nov/1980 05:50 LT (payload 33.010 [*Kopp et al.*, 1985a]), and 03/Aug/1982 01:32 LT (payload S37/P [*Kopp et al.*, 1984]). And the last two were launched from Red Lake (50.9° N, Canada), on 24 and 26/Feb/1979 11:55 LT (payloads 18.020 and 18.021, [*Kopp*, 1997]). The SO^+ observations have an uncertainty of the order of 100% [*Swider et al.*, 1979] and may contain interferences from the ion cluster $NO^+.(H_2O)$ as discussed below.

These eight rocket flights have been selected on the basis of showing signal at m/z = 48 (SO^+) above the noise, and all occurred in daytime or twilight conditions. The nighttime/daytime distinction is important because the $[O_2^+]/[e^-]$ ratio is different in the absence of sunlight [*Ogawa and Shimazaki*, 1975] and, as we have discussed above, O_2^+ and electrons control the source and sink of SO^+. The ratio of O_2^+ to electron densities is more important than their absolute densities, and therefore enhanced auroral activity (payload S37/P) should not have a very large impact on the SO^+ number density under the assumption of electrical neutrality (i.e. $[e^-] = [O_2^+] + [NO^+] + [Fe^+] + [Mg^+]\ldots$).

Geometric means of the SO^+ profiles are calculated due to the sparse data set available. The agreement between the S-MIF simulation and the observations is remarkably good considering the small number of observations and that rocket profiles are snapshots of the meteoric ion layers for ~20 s duration, and therefore reflect the particular state of the atmosphere in that narrow time window. We have not attempted to adjust the sulfur input to match the observations. In summer the S-MIF simulation overestimates the peak SO^+ number density by a factor of ~3, while the S-MIF/3 simulation matches better the observations, excluding the two sporadic layers shown, which correspond to a single rocket profile. Note that for the S-MIF/3 simulation, the corresponding SO layer in **Figure 3** is less dense by a factor of 3, i.e. peaking at 5×10^4 molecule cm^{-3} rather than 1.5×10^5 molecule cm^{-3}. In winter the situation is less clear, with the S-MIF simulation matching better the peak of the SO^+ layer. The two simulations bracket the SO^+ observations reasonably well at the altitude where the peak of the layer is expected.

In order to compare with SO_2 MIPAS observations between 15 and 45 km, the model output was degraded to the vertical resolution of the instrument by convolving it with a variable width Gaussian function, where the width is given by the altitude-dependent vertical resolution. Typical values for the vertical resolution are 3.5–4 km at 20 km, 4–5 km at 30 km and 6–10 km at 40 km altitude [*Höpfner et al.*, 2013]. Zonal averages of the simulated SO_2 fields were also calculated for the same latitudinal bands as the observations. **Figure 11** shows the resulting seasonally-averaged SO_2 contour plots for the S-MIF/3 simulation (left column) and the reference simulation (middle column), together with the MIPAS data (right column). The model captures the main features of the observations below 30 km, including the tropical stratospheric maximum and the polar winter descent of SO_2 from the mesosphere. However, both the reference and the S-MIF/3 simulations (and also the S-MIF simulation, not shown) fail to reproduce the elevated mixing ratios in the high stratosphere at tropical and

406 mid-latitudes. Furthermore, the S-MIF/3 simulation overestimates SO_2 in the winter pole
407 above 35 km (**Figure 12**).

408 Measurements of H_2SO_4 in the stratosphere are scarce. None is available over the southern
409 polar regions where the impact of meteoric sulfur would be the largest. A number of mid-
410 latitude stratospheric H_2SO_4 balloon-borne mass spectrometric measurements have been
411 reported, which have been compiled by Mills et al. [2005b]. **Figure 13*a*** compares the
412 geometric average of the available measurements at 43º N carried out in September and
413 October to the average profiles at the same latitude obtained from the CESM1-WACCM
414 reference and S-MIF runs (the differences between the S-MIF and S-MIF/3 results in the
415 upper stratosphere at low and mid-latitudes is small, and therefore only the S-MIF results are
416 shown). The model does a fairly good job in reproducing the average H_2SO_4 profile below 35
417 km, but largely overestimates the observations above this altitude. The difference between the
418 reference and S-MIF runs is negligible. For comparison, the average MIPAS SO_2 profile
419 between 40º and 50º N for September-November 2002-2012 is shown in **Figure 13*b***. The
420 model underestimates the observations for all altitudes above 25 km. The disagreement is
421 particularly dramatic at 32 km, where the model predicts a minimum. Smoothing the data
422 with the instrument vertical resolution helps to bring the model closer to the observations, but
423 not close enough.

424 CN observations (R > 3 - 10 nm, depending on pressure) up to 35 km height have been
425 carried out at McMurdo (Antarctica, 78º S) from the mid-1980s [*Campbell and Deshler*,
426 2014]. **Figure 14** compares the September monthly averages of the observed CN number
427 densities with the corresponding modeled vertical profiles for R > 3 nm and R > 10 nm for
428 the reference, the S-MIF and the S-MIF/3 simulations (profiles for other months are
429 compared in **Figure S6**). Note that a rigorous comparison would require convolving the

modeled sulfate aerosol number density for all bins with the dependence of the radius cut-off of the instrument with pressure. This function is unknown, but the rule-of-thumb is that the observations have a cut-off radius close to 3 nm below ~20 km (50 hPa), increasing to 10 nm at higher altitudes.

3.4. Contribution to the sulfur burden in the MLT, mesosphere and stratosphere

OCS is the most abundant sulfur-bearing molecule in the lower atmosphere and its vertical transport controls the stratospheric sulfur budget and the aerosol loading in periods of low volcanic activity [*Brühl et al.*, 2012]. The injection rate of active sulfur from OCS into the stratosphere is calculated from the photolysis rate of OCS and the reaction rates of OCS with $O(^3P)$ and OH, which are the major OCS loss processes in the stratosphere and generate a global sulfur flux into the stratosphere of 135 t S d^{-1}. The bulk of the OCS stratospheric loss occurs by photolysis and reaction with $O(^3P)$ in middle and low latitudes (< 50º) between 20 and 35 km. Explosive volcanic eruptions also inject considerable amounts of SO_2 into the stratosphere [*Mills et al.*, 2016]. Eruptions with volcanic explosive index (VEI) equal or larger than 4 [*Newhall and Self*, 1982] inject into the stratosphere a few percent of the SO_2 that they emit, depending on the latitude where the eruption takes place. In the 2002-2012 period (length of the MIPAS SO_2 record) the average SO_2 stratospheric injection was 560 t S d^{-1} according to the inventory of volcanic emissions implemented in WACCM by Mills et al. [2016]. An assumed flux of extra-terrestrial sulfur into the MLT of 3.0 t S d^{-1} is therefore 2 orders of magnitude smaller than the fluxes into the stratosphere from below. However, the mesospheric SO_2 mixing ratio fields plotted in **Figure 4** show that meteoric sulfur is focused into the polar vortices by the meridional circulation. Thus, the relative contribution of the S-MIF to the sulfur budget of the middle and upper stratosphere (25 - 50 km) at high latitudes is disproportionately larger than indicated by comparison of the global fluxes inputs. **Figure 2*b***

compares the contribution to the sulfur budget of meteoric and surface sources at different altitudes for six different latitudinal zones. It can be seen that the contribution of meteoric sulfur to the total gas phase sulfur density in the upper stratosphere increases towards the poles, reaching up to 35 % at 30 km over the southern hemisphere polar region in the S-MIF simulation (23% in the S-MIF/3 simulation).

4. Discussion

4.1. Sulfur in the MLT and the lower mesosphere

Besides the question of whether extra-terrestrial materials impact atmospheric radiative transfer and chemistry, the meteoric sulfur source is interesting because it dominates the sulfur budget above the mesopause. The sulfur MIF has a number of important consequences, namely the formation of an SO layer in the MLT, with a weaker SO^+ counterpart (**Figure 3**), and a substantial increase of the SO_2 density in the mesosphere (on average by a factor of 2 at ~65 km, for the S-MIF).

The mass spectrometric observations of putative sulfur ions in the MLT carried out by Narcisi [1969], Zbinden [1975] and co-workers stimulated laboratory studies on sulfur chemistry [*Fehsenfeld and Ferguson*, 1973] and subsequent steady-state calculations of the sulfur budget using the reported rate constants [*Swider et al.*, 1979]. These calculations are essentially in agreement with the modeling results presented here regarding S, S^+, SO and SO^+. The meteoric sulfur layer between 90 and 100 km (**Figure 3**) is dominated by SO, with $[SO] > [SO_2] > [SO^+] > [S] >> [SO2^+] > [S^+]$. The low density of SO^+ observed by rocket-borne mass spectrometry (**Figure 10**) stems from the fast neutralization of SO^+ by dissociative recombination, and the fast reaction of S with O_2 [*Davis et al.*, 1972]. The main source of SO^+ is charge transfer between SO and O_2^+. CESM1-WACCM has been previously

shown to capture the seasonal variation of electrons [Feng et al., 2013], and agrees well with the observed electron and O_2^+ number densities at 95 km ($[e^-] = 10^4 - 10^5$ cm^{-3}).

The seasonal behavior of SO and SO_2 is driven by SO_2 photolysis and the reaction between SO and O_2. Because SO^+ is tied to SO, it follows a similar seasonal variation. The SO^+/SO ratio also depends on the seasonal variation of O_2^+ and e^-. SO_2 is a comparatively inert reservoir molecule which is transported to lower atmospheric layers. The lack of chemical sinks implies a very long lifetime of SO_x (= SO + SO_2), which therefore shows a spatio-temporal distribution determined by transport. This explains why the seasonal behavior of SO_x does not reflect the seasonal variability of the MIF, which peaks in the autumn hemisphere at high latitudes [*Feng et al.*, 2013]. The abundance of S-containing species in the mesosphere and upper stratosphere is driven by the residual circulation, with winter-poleward transport at mesopause heights and downwelling around the winter pole. The calculated atmospheric profiles in the winter polar regions depend on the model-resolved residual circulation, and therefore the conclusions of the present study rely on how well transport is represented in CESM1-WACCM. Global observations of zonal winds and mesospheric temperature have been used previously for validation purposes [*Garcia et al.*, 2007; *Richter et al.*, 2010; *Smith*, 2012; *Feng et al.*, 2013]. Feng et al. have demonstrated good agreement between CESM1-WACCM simulations and zonal mean temperature and wind from the COSPAR International Reference Atmosphere (CIRA) [*Fleming et al.*, 1990]. Similarly, Smith [2012] compared WACCM temperature and zonal mean wind with measurements of the Sounding of the Atmosphere using Broadband Emission Radiometry (SABER) instrument and the UARS Reference Atmosphere Project (URAP) climatology [*Swinbank and Ortland*, 2003]. The distribution of advected tracers such as CO, CO_2, NO, O or SF_6 also provides a way for validating the strength and structure of the mean circulation in CESM1-WACCM [*Smith, A K et al.*, 2011; *Garcia et al.*, 2014; *Kovács et al.*, 2017].

Before comparing rocket-borne SO^+ observations and model output, care needs to be taken when assigning m/z = 48, as the ion cluster $NO^+.(H_2O)$ has the same mass-to-charge ratio and peaks at the transition height between 70 and 90 km where there is a temperature minimum with low electron density and atomic oxygen [*Kopp et al.*, 1985b]. To avoid contamination of the m/z = 48 signal from $NO^+.(H_2O)$, only data above 94 km has been considered in **Figure 10**. Considering the large uncertainties in the observations, the S-MIF model results are reasonably close to the SO^+ rocket observations. The S-MIF run overestimates the summer peak SO^+ abundance by a factor of ~3. The S-MIF/3 simulation indicates that the number densities of MLT sulfur species are indeed proportional to the meteoric sulfur input. Scaling down the sulfur input by a factor of 3 (S-MIF/3) results in a peak [SO] ~ 5×10^4 cm^{-3}. For reference, the peak concentrations of reactive sodium, iron, magnesium and silicon around 90 km are respectively [Na] + [Na^+] ~ 5×10^3 cm^{-3} [*Marsh et al.*, 2013a], [Fe] + [Fe^+] ~ 2×10^4 cm^{-3} [*Feng et al.*, 2013], [Mg] + [Mg^+] ~ 5×10^3 cm^{-3} [*Langowski et al.*, 2015] and [SiO] + [Si^+] ~ 1×10^4 cm^{-3} [*Plane et al.*, 2016]. Comparison of MLT densities does not translate directly into input rate ratios because of differences in the chemistries and ablation height profiles of the elements, but it highlights the higher abundance of gas-phase sulfur in the MLT compared to most other elemental constituents of meteoroids, which results from the combination of a high sulfur abundance in cosmic dust, the relative volatility of sulfur, and a lack of chemical sinks.

The relatively high density of SO in the MLT raises the question of whether direct detection of it in the MLT is feasible, e.g. by using its B-X or A-X transitions in absorption or fluorescence. The strong B-X transition [*Danielache et al.*, 2014] appears too deep in the UV (200 - 230 nm) and has absorption cross sections insufficiently large (peak at 2.7×10^{-17} cm^2 at 0.08 nm resolution) [*Phillips*, 1981; *Whyte and Phillips*, 1982] to enable observation by absorption, even in occultation (attenuation ~ 1×10^{-7} km^{-1}). The SOFIE instrument on the

AIM satellite has been used by Hervig et al. [2009] to measure the weak extinction caused by MSP using solar occultation, but this is only possible from 330 nm to longer wavelengths. Fluorescence from the B state occurs for $v' \leq 2$, since higher vibrational levels pre-dissociate. The $v' - 0$ bands with $v' \leq 2$ are located around 240 nm and their absorption cross sections are smaller than 1×10^{-18} cm^2 [*Danielache et al.*, 2014], which precludes using ground-based lidar. A more promising approach may be attempting a retrieval of SO B-X and A-X fluorescence from dayglow spectra recorded by satellite-borne spectrometers such as SCIAMACHY (see e.g. normalized radiance spectra reported by Scharringhausen et al. [2008]), in a similar manner to observations of cometary tails carried out by the International Ultraviolet Explorer satellite [*Wallis and Swamy*, 1988; *Kim and A'Hearn*, 1991].

The possible existence of a mesospheric sulfate aerosol layer has been previously suggested by Mills et al. [2005a], who considered injection of H_2SO_4 in the summer polar mesosphere resulting from evaporation of H_2SO_4 from uplifted SSA. As shown in **Figure 2*a***, meteoric sulfur does not form additional H_2SO_4 in the MLT, because of the low pressure and low water (and hence OH) concentration. The main forms of meteoric sulfur are SO and SO_2, which are non-condensable species under MLT conditions. Therefore, the impact of the meteoric sulfur input on such a mesospheric layer is most likely negligible.

4.2. Meteoric sulfur in the upper stratosphere.

Present day cosmic dust ablation has been considered to be a very small source of sulfur for the stratosphere. Turco et al. [1981] estimated a mass input rate of meteoric sulfur to the stratosphere of ≤ 5.5 t S d^{-1} (*cf.* 3.0 t S d^{-1} in our S-MIF simulation) compared to a mass input rate of 822 t S d^{-1} from surface sources. Cziczo et al. [2001] suggested an input range of 1.4 - 4.7 t S d^{-1}, representing less than 2% of the of the total stratospheric sulfur budget. More developed estimates of surface and meteoric sources of sulfur are now available and have

551 been considered in the present study. Court and Sephton [2011] speculated that atmospheric
552 dynamics could enhance the impact of the meteoric source compared to volcanism. However,
553 the only way of rigorously answering this question is by using a global chemistry-climate
554 model. Our calculations show that SO_2 is transported by the mesospheric meridional
555 circulation into the winter polar vortex, before descending into the stratosphere. That is, the
556 potential stratospheric impacts are mostly confined to the polar regions, where the focusing
557 enhances the importance of meteoric sulfur relative to surface sources above 25 km at high
558 latitudes. Thus, meteoric sulfur may contribute to the buildup of the spring-time SSA layer
559 over Antarctica, and thus have the potential to influence polar stratospheric cloud formation
560 and therefore ozone loss.

561 Although the purpose of this study is not to improve the agreement between the standard
562 CESM1-WACCM predictions [*Campbell et al.*, 2014; *Mills et al.*, 2016] (which are
563 equivalent to our reference simulation) and the available observations of sulfur species, the
564 striking disagreement with MIPAS SO_2 and balloon H_2SO_4 observations in the upper
565 stratosphere at middle and low latitudes (**Figures 11** and **13**) led us to investigate whether
566 meteoric sulfur could ameliorate the situation. Because of the focusing of meteoric sulfur
567 inside the polar vortices, the S-MIF does not improve the agreement with MIPAS, and as
568 shown in **Figure 13** the H_2SO_4 and SO_2 profiles at 43° N for the reference and the S-MIF
569 simulations are almost identical.

570 Uptake on MSPs, which is not included in these simulations, has been invoked previously to
571 explain the poor agreement with H_2SO_4 above 35 km [*Turco et al.*, 1981; *Mills et al.*, 2005b;
572 *Saunders et al.*, 2012; *Hervig et al.*, 2017]. Brühl et al. [2015] carried out simulations with
573 the EMAC atmospheric chemistry-climate model, suggesting that a meteoric dust sink for
574 H_2SO_4 is required to reproduce the observed distribution of SO_2 with latitude and season at

575 40 km; ignoring this process would lead to overestimation of SO_2 during high latitude winter.
576 However, enhanced near-infrared photolysis of H_2SO_4, which has not yet been demonstrated
577 theoretically nor experimentally, had to be considered by Brühl et al. to explain the SO_2
578 observations at low latitudes at 40 km, and ignoring this resulted in underestimation of SO_2
579 by 50 pptv. This is consistent with our results, which indicate that at mid-latitudes the excess
580 of modeled H_2SO_4 is matched by the deficit of modeled SO_2 above 35 km, suggesting that
581 despite using the best current knowledge of H_2SO_4 absorption cross sections and pressure-
582 dependent photolysis quantum yields, there is still something missing in the photochemical
583 scheme. Note that we have ruled out H_2SO_4 photolysis via the $v \leq 3$ OH stretching overtones
584 because they appear to be below the dissociation threshold. Ongoing work at the University
585 of Leeds using the UM-UKCA model [Dhomse et al., 2014] with state-of-the-art sulfur
586 sources and photochemistry shows that uptake of H_2SO_4 on MSP may indeed help to explain
587 the general model overestimation of H_2SO_4 above 40 km (Graham Mann, pers. comm.), but
588 at middle and low latitudes the simulated SO_2 is substantially reduced with respect to the
589 MIPAS observations when MSPs are included, which may suggest a missing process for
590 converting H_2SO_4 into SO_2. Overestimation of SO_2 mixing ratios by MIPAS retrievals at
591 middle and low latitudes between 12 and 20 km [*Höpfner et al.*, 2015] has also been
592 suggested by comparing recent in situ observations with an aircraft-borne laser induced
593 fluorescence instrument and remote sensing observations using the Atmospheric Chemistry
594 Experiment Fourier Transform Spectrometer (ACE-FTS) [*Rollins et al.*, 2017]. However, it
595 must me pointed out that the MIPAS and ACE-FTS uncertainty ranges and the short time
596 scale variability range of the in situ measurements contain the corresponding CESM1-
597 WACCM SO_2 averaged profiles, as noted by Rollins et al. [2017]. Other stratospheric SO_2
598 profiles derived from remote sensing observations have been obtained with the ATMOS

599 instrument [*Rinsland et al.*, 1995] and are in general significantly higher than the MIPAS
600 observations above 30 km [*Höpfner et al.*, 2013].

601 On the other hand, the CESM1-WACCM simulations of H_2SO_4 below 35 km and SO_2 below
602 25 km appear reasonable: smoothing the model output with the altitude-, latitude- and time-
603 dependent vertical resolution matrix of the MIPAS SO_2 observations helps bringing the
604 modeled SO_2 around the minimum at 32 km into better agreement with the observations.
605 However, the uncertainty of the MIPAS retrieval between 20 and 35 km at middle and low
606 latitudes is large (because the signal is low), and the observations in this altitude-latitude
607 range should not be over-interpreted. As a summary, it can be stated that the disagreement
608 appears to be a combination of shortcomings in the model photochemistry and issues with the
609 MIPAS retrieval under very low signal conditions.

610 The MIPAS observations at high latitudes (70°-90°) in the winter hemisphere are less
611 uncertain than at lower latitudes and seem to be reliable from 45 km down to 20 km due to
612 the descent of enhanced upper stratospheric SO_2 concentrations. Comparison to the SO_2
613 VMRs from the reference run (**Figure 11**) shows that in the polar regions the simulations are
614 not too far from the observations between 35 and 40 km, although the predicted SO_2 polar
615 enhancement is latitudinally narrower and restricted to a higher altitude range than in the
616 observations. The S-MIF simulation predicts 250 pptv SO_2 on top of the 100 pptv baseline
617 predicted by the reference run at 45 km in winter for 70ºS - 90ºS (**Figure 12**). This means
618 that the meteoric sulfur at 45 km is a factor of ~5 larger than 1σ of the observations for that
619 zonal band and season (50 pptv). The quoted uncertainty of the retrieval is of the order of 10
620 pptv at 45 km. The S-MIF/3 simulation predictions on the other hand overlap with the
621 variability range of the observations, although it still overestimates the observations in the
622 southern hemisphere polar region above 37 km.

From the point of view of the SSA layer, the only instance where the input of meteoric sulfur could be potentially observed is in spring at high latitudes in the southern hemisphere, when the $R > 3$ nm CN number density increases by up to 70% at 30 km and about 40% at 25 km in the S-MIF simulation. **Figure 14** shows that the calculated profile for $R > 3$ nm from the S-MIF run (red dots) is just about compatible with the observations of the sulfate CN spring layer at McMurdo below 25 km (where he observed CN can be considered to have $R > 3$ nm), but generates number densities of $R > 10$ nm CN above 25 km (red triangles) that are outside the observed range of variability. This is consistent with the overestimated SO_2 mentioned above, since at the onset of the polar spring the extra SO_2 is converted into H_2SO_4, which undergoes binary nucleation with water to form SSA. In fact, the S-MIF/3 simulation generates number densities of R > 10 nm CN above 25 km which are closer to and within the variability range of the observations. In summary, the S-MIF simulation exercise shows that the CN polar layers are sensitive to extraterrestrial sulfur, and may have been influenced in the past by events within the solar system causing enhanced rates of cosmic dust infall. With the assumption that the CN layers are formed only by the binary H_2O-H_2SO_4 homogeneous nucleation, a sulfur input of 1 t S d^{-1} (S-MIF/3) appears to be compatible with the available CN observations.

There is increasing observational evidence supporting the uptake of H_2SO_4 on MSPs and the formation of mixed MSP-sulfate particles in the lower mesosphere and the upper stratosphere [*Neely et al.*, 2011; *Saunders et al.*, 2012; *Campbell and Deshler*, 2014; *Murphy et al.*, 2014; *Hervig et al.*, 2017]. Given the uncertainties surrounding the role of MSPs as condensation nuclei of sulfate particles, we have not included MSP-sulfate interactions in the model simulations presented here. The presence of MSPs and uptake of H_2SO_4 on them will tend to reduce the number density of sulfate aerosol formed by binary H_2SO_4-H_2O nucleation in the upper part of the Junge layer, where mixed MSP-sulfate aerosol would be abundant. This

may then reduce the impact of meteoric sulfur on homogeneously nucleated SSA deduced from our calculations with CARMA, and therefore may help to accommodate a sulfur input larger than 1 t S d^{-1}. The loss of gas-phase sulfur on MSP, which in the model calculations mentioned above results in a decrease of SO_2 above 40 km, may allow a larger S-MIF as well. In the present study, we are mainly concerned about the differences between model runs with and without meteoric sulfur using the best available knowledge on sulfur atmospheric chemistry. Finding closure to the atmospheric sulfur budget is beyond the scope of this study.

4.3. Constraining the cosmic dust input into the Earth's atmosphere.

The results of the S-MIF simulation with an injection of 3.0 t S d^{-1} overestimate the observed abundances of a variety of sulfur species in different regions of the atmosphere. The S-MIF/3 simulation predicts SO^+, SO_2 and CN profiles which are more consistent with observations. Therefore, sulfur observations in the upper stratosphere and above constrain consistently the input of meteoric sulfur to approximately 1.0 t S d^{-1}.

There are three main reasons why the input of sulfur may be overestimated by the abundance-scaled Na MIF: *i*) a depletion of sulfur relative to sodium in IDPs ($\delta/\gamma < 1$ in equation E1), *ii*) a less efficient ablation of sulfur compared to sodium ($\phi_S/\phi_{Na} < 1$), or *iii*) the sodium input itself is overestimated. Of these three explanations we favor the first, since the sodium input is now well characterized by lidar observations [*Gardner et al.*, 2016], and a lower ablation efficiency of sulfur with respect to sodium seems unlikely based on laboratory experiments with heated meteorites [*Jurewicz et al.*, 1993; *Greshake et al.*, 1998]. In CC meteorites, the major carriers of sulfur are sulfate minerals, which are more refractory than sulfides (*Burgess et al*., 1991). However, sulfates are not found in MMs (*Jessberger et al*., 2001), and have been observed only as minor components in some stratospheric IDPs (*Zolensky and*

672 *Lindstrom*, 1992). Therefore, it can be inferred that sulfur is present mostly in the form of
673 iron and nickel sulfides in cosmic dust, which evaporate at lower temperatures.

674 There is evidence supporting enrichment of Na relative to all other major elemental
675 constituents in cosmic dust, meteor showers and freshly ejected cometary particles [*Trigo-*
676 *Rodriguez and Llorca*, 2007; *Schulz et al.*, 2015; *Carrillo-Sánchez et al.*, 2016]. *Carrillo-*
677 *Sanchez et al*. [2016] needed an enrichment factor of γ = 2.5 of Na with respect to Fe to
678 explain the relative vertical fluxes of Na and Fe atoms in the upper mesosphere. In fact, in
679 order to obtain the same cosmic dust input rate (CDIR) from the measured inputs of meteoric
680 sodium [*Gardner et al.*, 2016] and iron [*Huang et al.*, 2015]:

681 $$CDIR = \frac{MIF}{\gamma \times x \times \phi}\Big|_X = \frac{0.34\ t\ Na\ d^{-1}}{\gamma \times 0.0047 \times 0.6} = \frac{2.5\ t\ Fe\ d^{-1}}{0.19 \times 0.3} = 44\ t\ d^{-1} \quad \text{(E2)}$$

682 Na must be enriched by a factor of γ = 2.7 ± 1.5. The CDIR in equation E2 is the ratio of the
683 MIF of a particular meteoric elemental constituent X to the product of the abundance of X in
684 cosmic dust, multiplied by its ablation efficiency. To evaluate E2 for sodium and iron we
685 have used estimated ablation efficiencies (Table 2) from experiments with the Meteor
686 Ablation Simulator [*Gómez Martín et al.*, 2017], and it has been assumed that IDPs are not
687 depleted in iron. The analogous equation for sodium and sulfur is then:

688 $$CDIR = \frac{0.34\ t\ d^{-1}}{\gamma \times 0.0047 \times 0.6} = \frac{1.0\ t\ d^{-1}}{\delta \times 0.041 \times \phi_S} = 44\ t\ d^{-1} \quad \text{(E3)}$$

689 This implies that $\delta \times \phi_S \leq 0.6$ when considering 1.0 t d^{-1} as an upper limit for the sulfur input,
690 which is consistent with $\phi_S \geq \phi_{Na} = 0.6$ and suggests that $\delta \leq 1$, i.e. that sulfur is chondritic
691 or slightly sub-chondritic in IDPs. The average sulfur ablated fraction derived from CI and
692 CM cosmic dust analogues is 0.8-0.9 [*Greshake et al.*, 1998; *Court and Sephton*, 2014] for
693 heating up to 1300 K during 10 to 15 s. Under the assumption of chondritic abundance of

694 sulfur in IDPs, an ablated fraction of 0.85 results in a CDIR = 29 t d^{-1}, which is consistent
695 with the 45% uncertainty of the CDIR value in equations E2 and E3. The laboratory
696 determinations of the ablated fraction of sulfur were carried out under conditions not entirely
697 relevant for the atmosphere. Although the heating curves were not reported, the duration of
698 the heating pulses (longer than 10 s) are somewhat long compared to predictions from meteor
699 physics calculations [*Love and Brownlee*, 1991]. It is therefore plausible that the atmospheric
700 ablated fraction is slightly smaller than the aforementioned experiments suggest. Future
701 laboratory measurements of the sulfur yield should be carried out under mass, size and entry
702 angle dependent heating profiles in order to calculate more representative integrated
703 atmospheric yields [*Bones et al.*, 2016; *Gómez Martín et al.*, 2017].

704 The only caveat to this interpretation is that the relative abundances of sodium and sulfur in
705 unmelted and scoriaceous MMs [*Kurat et al.*, 1994; *Genge et al.*, 1997] and stratospheric
706 IDPs [*Schramm et al.*, 1989; *Arndt et al.*, 1996] are close to chondritic (**Figure S2**), and in
707 order to explain such relative abundances, an original enrichment of sodium could only be
708 compensated by a lower ablation efficiency of sulfur, which as mentioned above seems
709 unlikely. Stratospheric IDPs may be asteroidal in origin (due to their slow entry speed) and
710 thus reflect a S/Na ratio closer to CI, but unmelted MMs have been shown to originate mostly
711 from cometary meteoroids [*Carrillo-Sánchez et al.*, 2016] and should reflect a depletion of
712 sulfur with respect to sodium (assuming they are not altered by weathering).

713 **4. Conclusions**

714 This study indicates that cosmic dust ablation is the major source of sulfur to the MLT and
715 the lower mesosphere, creating a layer of SO peaking at 90 km with a higher number density
716 than the meteoric Fe layer. A photochemical equilibrium is established between SO and SO_2
717 in the MLT, where the partitioning changes seasonally with solar illumination. The number

718 density of SO is predicted to be high enough that it may be detectable through spectroscopic
719 observation of the dayglow. Because of the lack of chemical sinks for SO_2 due to low
720 pressure and hydroxyl radical density in the mesosphere, most of the injected sulfur is
721 transported into the upper stratosphere as SO_2, where it contributes to the nucleation of
722 sulfate aerosol in polar spring. The sulfate stratospheric CN layer is very sensitive to the
723 meteoric injection rate: a moderate rate of 3.0 t S d^{-1} results in the model overestimating polar
724 springtime CN above 20 km compared with observations. The present day input rate needs to
725 be on the order of 1.0 t S d^{-1} to be consistent with all the observations available, including
726 SO^+ in the MLT, and SO_2 and CN in the middle and upper stratosphere. An enhanced input
727 of cosmic dust, such as during the Late Heavy Bombardment or a close encounter with a
728 comet, would have a significant impact on the sulfate layer at high latitudes. The present day
729 estimate of 1.0 t S d^{-1} translates into similar overall input rates of cosmic dust that were
730 deduced from the measured Fe and Na fluxes, supporting the superchondritic abundance of
731 Na suggested in previous work, and implying a chondritic abundance of sulfur in cosmic dust
732 and a similar ablated fraction of meteoric Na and S. Future refinements of the estimated input
733 rate of meteoric sulfur presented here should address the impact of heterogeneous nucleation
734 of H_2SO_4 by MSPs.

735

736 **Acknowledgements**

737 This work was supported by the European Research Council (project 291332 - CODITA).
738 The rocket flight data was kindly provided by E. Kopp (University of Bern). The SO_2 dataset
739 retrieved at KIT/IMK is available at http://www.imk-asf.kit.edu/english/308.php. The latest
740 version of CESM1-WACCM is available at https://svn-ccsm-
741 models.cgd.ucar.edu/cesm1/tags/cesm1_5_beta06/. We would like to thank Francis Vitt at
742 NCAR for the CESM1-WACCM model development. The National Center for Atmospheric

743 Research is sponsored by the National Science Foundation. Any opinions, findings, and
744 conclusions or recommendations expressed in the publication are those of the author(s) and
745 do not necessarily reflect the views of the National Science Foundation. The model output
746 generated for this work has been archived at Leeds University PETAL
747 (http://www.petal.leeds.ac.uk).

748 **Table 1.** Sulfur ion-neutral and dissociative recombination (DR) reactions.

#	Reaction	ΔH_{298}/kJ mol^{-1} [a]	k/ $\times 10^{-10}$ cm^3 s^{-1}	Reference
1	$S + O_2^+ \rightarrow S^+ + O_2$	-164.9	1.0	same as $N + O_2^+$, branching 50% [b]
2	$S + O_2^+ \rightarrow SO^+ + O$	-194.2	1.0	same as $N + O_2^+$, branching 50% [b]
3	$S + N_2^+ \rightarrow S^+ + N_2$	-503.4	1.4	same as $O + N_2^+$ [b]
4	$SO + O_2^+ \rightarrow SO^+ + O_2$	-171.2	$18\times(T/300)^{-0.5}$	dipole-ion calculation [c]
5	$SO + N_2^+ \rightarrow SO^+ + N_2$	-509.8	$19\times(T/300)^{-0.5}$	dipole-ion calculation [c]
6	$SO_2 + N_2^+ \rightarrow SO_2^+ + N_2$	-311.6	$5.0\times(T/300)^{-0.5}$	experimental 298 K, [b] T dependence dipole-ion [c]
7	$S^+ + O_2 \rightarrow SO^+ + O$	-29.3	$0.185\times(T/300)^{-0.6}$	experimental 298 K, [b] T dependence as $O^+ + O_2 \rightarrow O_2^+ + O$ 20-300 K
8	$S^+ + O_3 \rightarrow SO^+ + O_2$	-420.3	$2.8\times(T/300)^{-0.5}$	dipole-ion calculation, [c] branching as for $Si^+ + O_3 \rightarrow SiO^+ + O_2$ (45%) [d]
9	$S^+ + O_3 \rightarrow SO + O_2^+$	-249.1	$2.8\times(T/300)^{-0.5}$	dipole-ion calculation, [c] branching as for $Si^+ + O_3 \rightarrow SiO + O_2^+$ (45%) [d]
10	$S^+ + O_3 \rightarrow SO_2^+ + O$	-274.8	$0.62\times(T/300)^{-0.5}$	dipole-ion calculation, [c] branching as for $Si^+ + O_3 \rightarrow SiO_2^+ + O$ (10%) [d]
11	$S^+ + NO \rightarrow S + NO^+$	-105.7	$3.3\times(T/300)^{-0.5}$	experimental 298 K [b] with T dependence dipole-ion [b]
12	$SO^+ + O_3 \rightarrow SO_2 + O_2^+$	-272.4	$5.3\times(T/300)^{-0.5}$	dipole-ion calculation, [c] branching as for $SiO^+ + O_3 \rightarrow SiO_2 + O_2^+$ (95%) [d]
13	$SO^+ + O_3 \rightarrow SO_2^+ + O_2$	-245.5	$0.28\times(T/300)^{-0.5}$	dipole-ion calculation, [c] branching as for $SiO^+ + O_3 \rightarrow SiO_2^+ + O_2$ (5%) [d]
14	$SO^+ + NO \rightarrow SO + NO^+$	-99.3	$1.8\times(T/300)^{-0.5}$	dipole-ion calculation [c]
15	$SO^+ + e^- \rightarrow S + O$	-471.1	$3800\times(T/300)^{-0.5}$	same as $SO_2 + e^-$ [e]
16	$SO_2^+ + O_2 \rightarrow SO_2 + O_2^+$	-26.9	2.65	experimental 298 K, [b] T independent
17	$SO_2^+ + NO \rightarrow SO_2 + NO^+$	-297.5	$0.7\times(T/300)^{-0.5}$	experimental 298 K, [b] T dependence dipole-ion [c]
18	$SO_2^+ + H \rightarrow SO^+ + OH$	-77.0	4.2	experimental 298 K, [b] T independent
19	$SO_2^+ + O \rightarrow SO^+ + O_2$	-145.6	4.2	same as $SO_2^+ + H$ [b]
20	$SO_2^+ + CO \rightarrow SO^+ + CO_2$	-179.3	$3.0\times(T/300)^{-0.5}$	experimental 298 K, [b] T dependence dipole-ion [c]
21	$SO_2^+ + e^- \rightarrow SO + O$	-639.6	$2300\times(T/300)^{-0.5}$	experimental with typical DR T dependence [e]
22	$SO_2^+ + e^- \rightarrow S + O + O$	-118.2	$1500\times(T/300)^{-0.5}$	experimental with typical DR T dependence [e]

749 [a] NIST Chemistry webbook [*Linstrom*, 2016] and references therein.
750 [b] An Index of the Literature for Bimolecular Gas Phase Cation-Molecule Reaction Kinetics [*Anicich*, 2003] and references therein.
751 [c] [*Georgievskii and Klippenstein*, 2005].
752 [d] [*Gómez Martín and Plane*, 2011].
753 [e] Dissociative Recombination [*Florescu-Mitchell and Mitchell*, 2006] and references therein.
754

Table 2. Estimated abundances of iron, sulfur and sodium in IDPs, calculated ablated fractions and observed meteoric metal fluxes.

	SPWW fractions (%) [d]	**Fe**	**S**	**Na**
CI&CM [a]	75	19.6	4.6	0.45
OC [b]	10	22.5	2.2	0.68
Anhydrous [c]	15	13.5	3.0	0.41
Weighted abundances (% wt.)		19.0	4.1	0.47
x_S/x_X (atom atom^{-1}) [e]		0.38		6.3
ϕ [f]		0.3-0.5	$\geq \phi_{Na}$	0.6-0.8
MIF (atom cm^2 s^{-1}) [g]		6×10^4		2×10^4
MIF (t d^{-1}) [g]		2.5 ± 1.1		0.34 ± 0.08

[a] Average of CI and CM % weight abundances [*Hutchison*, 2004]
[b] Average of H, L and LL % weight abundances [*Hutchison*, 2004]
[c] % weight abundances in coarse stratospheric IDPs [*Schramm et al.*, 1989]
[d] Contribution of different meteoritic compositional groups to the 2000 South Pole Water Well MM Collection [*Taylor et al.*, 2012]
[e] Ratio of elemental sulfur abundance (% atom) to abundance of element X (X = Fe, Na)
[f] Ablated fractions of Fe and Na from the meteor ablation simulator (MASI) [*Gómez Martín et al.*, 2017] weighted with the Planck or the IRAS mass distributions [*Carrillo-Sánchez et al.*, 2016].
[g] Fluxes from [*Huang et al.*, 2015; *Carrillo-Sánchez et al.*, 2016; *Gardner et al.*, 2016]

767 **Figures**

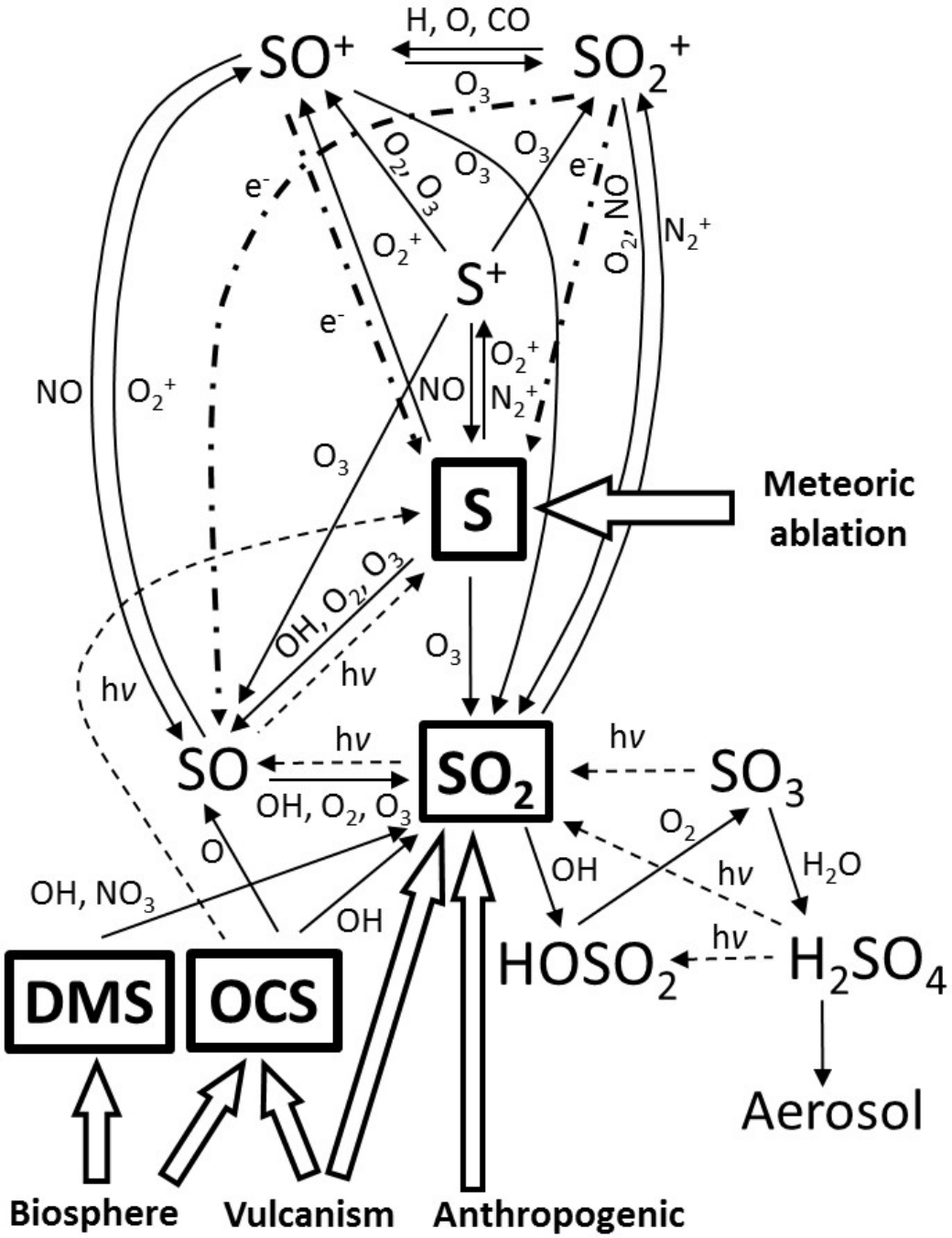

768

769 **Figure 1.** Atmospheric sulfur cycle. Solid, dashed and dash-dotted lines indicate respectively
770 chemical, photolysis and electron recombination reactions.

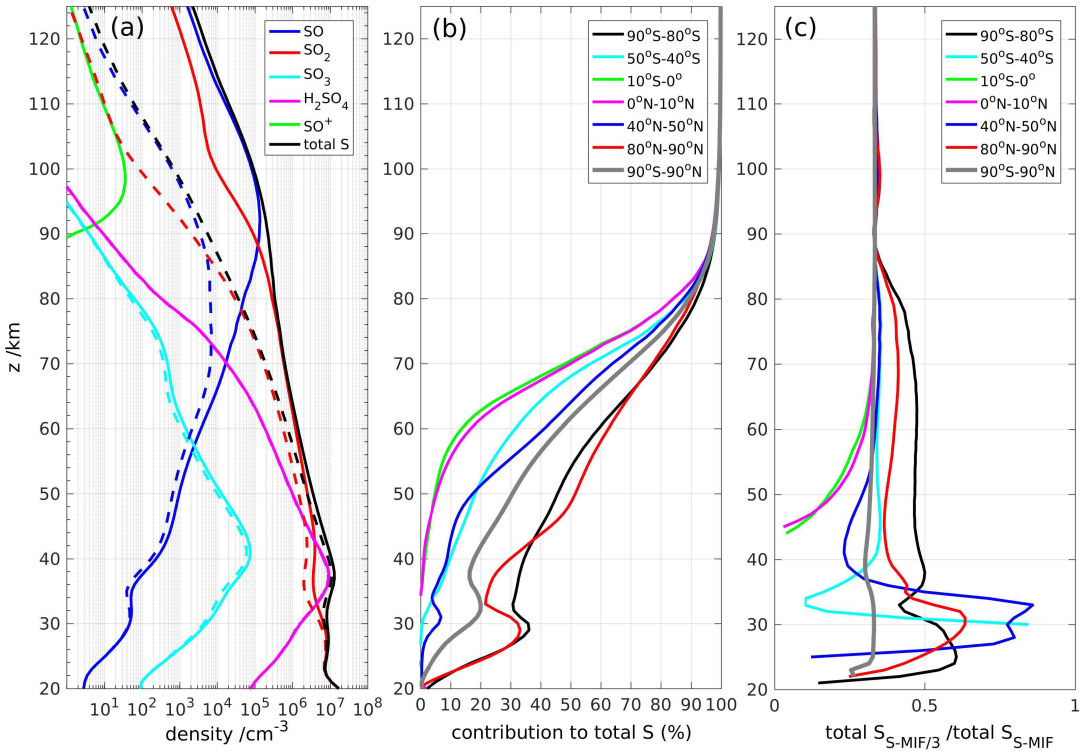

771

772 **Figure 2.** Panel *a*: Number density annual global averages vs. altitude for the major sulfur-
773 containing species. Dashed lines correspond to the reference simulation and solid lines to the
774 S-MIF simulation. Panel *b*: contribution of meteoric sulfur (S-MIF run) to the total gas phase
775 sulfur number density as a function of altitude for six different latitudinal zones (colors) and
776 the global average (grey). Panel *c*: ratio of total gas phase sulfur in the S-MIF/3 simulation to
777 total gas phase sulfur in the S-MIF simulation for different latitudinal zones and the global
778 average (grey).

779

780

781

782

783

784

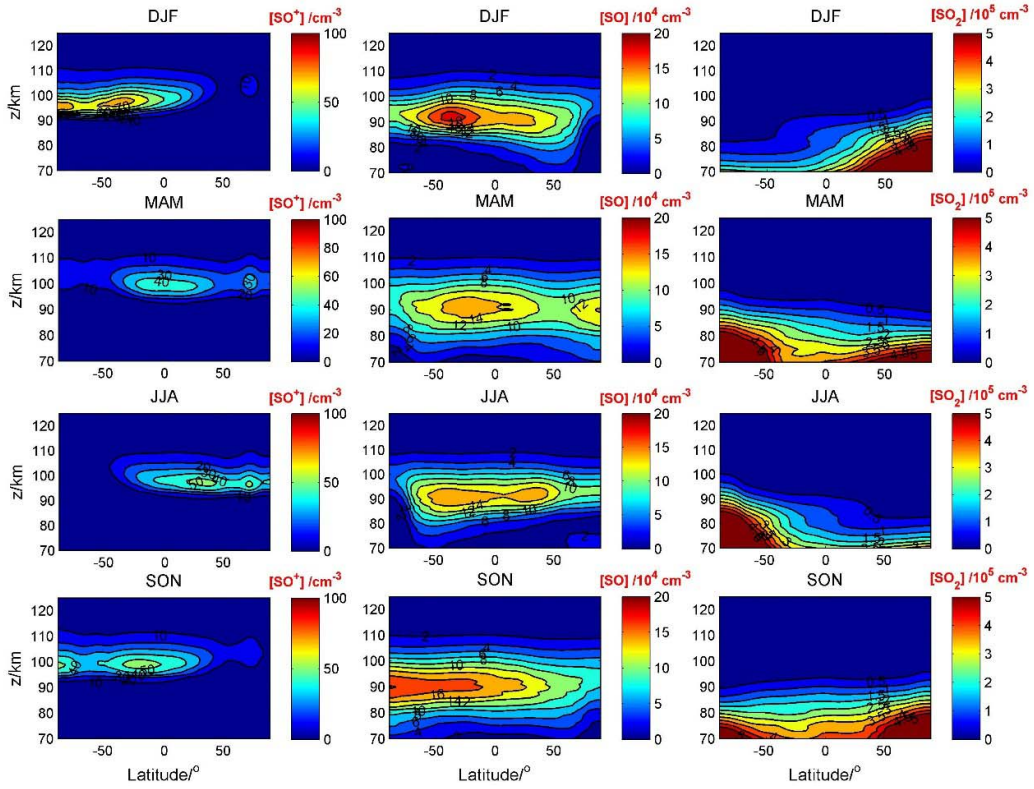

Figure 3. Number density seasonal averages vs altitude and latitude of SO^+, SO and SO_2 in the MLT from the S-MIF simulation (DJF: December-January-February; MAM: March-April-May; JJA: June-July-August; SON: September-October-November). The S-MIF/3 simulation produces identical distributions, but with number densities smaller by a factor of 3.

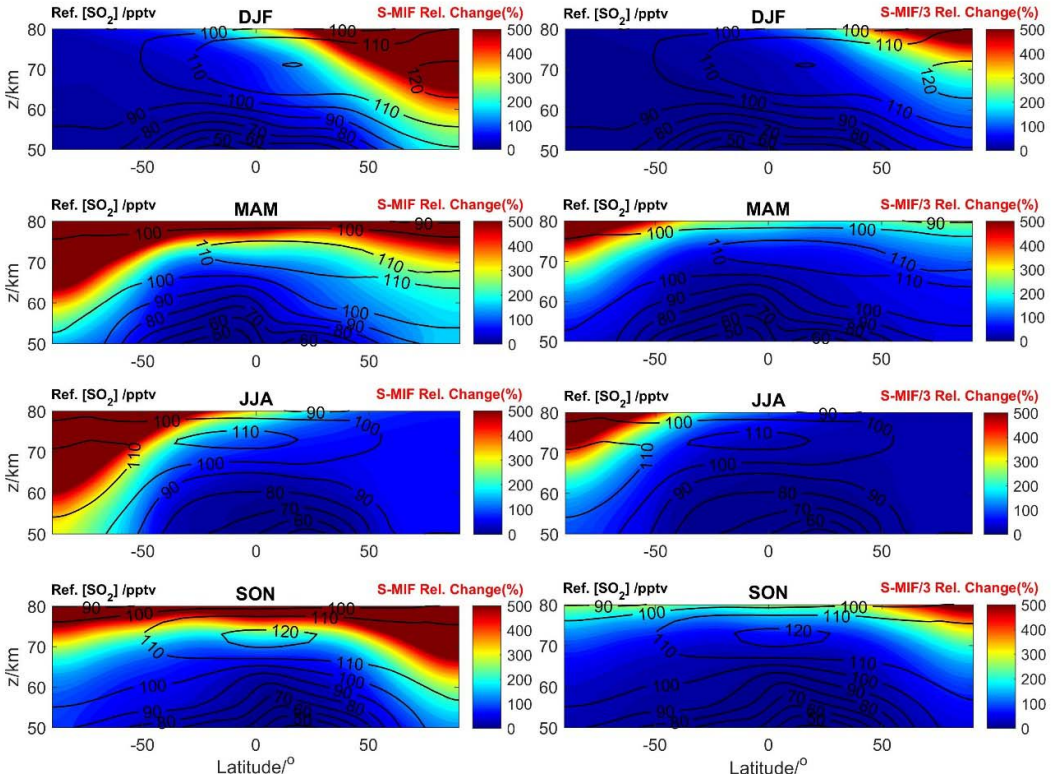

792

793 **Figure 4** Volume mixing ratio (VMR) seasonal averages vs altitude and latitude of SO_2 in the
794 mesosphere. Contour black lines: VMR for the reference simulation (without meteoric
795 sulfur). Filled color contours: percent change by adding meteoric sulfur (left column: S-MIF
796 simulation; right column: S-MIF/3 simulation).

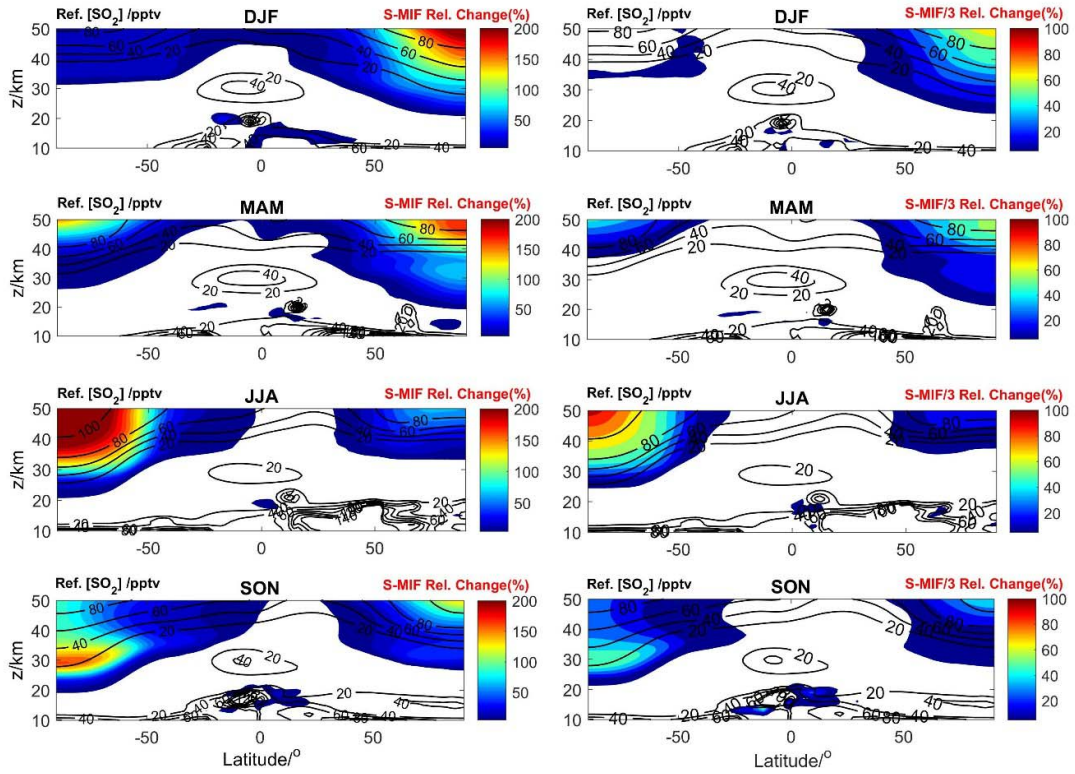

Figure 5. VMR seasonal averages vs. altitude and latitude of SO_2 in the stratosphere. Contour lines: VMR for reference simulation. Filled color contours: percent change by adding meteoric sulfur (left column: S-MIF simulation; right column: S-MIF/3 simulation).

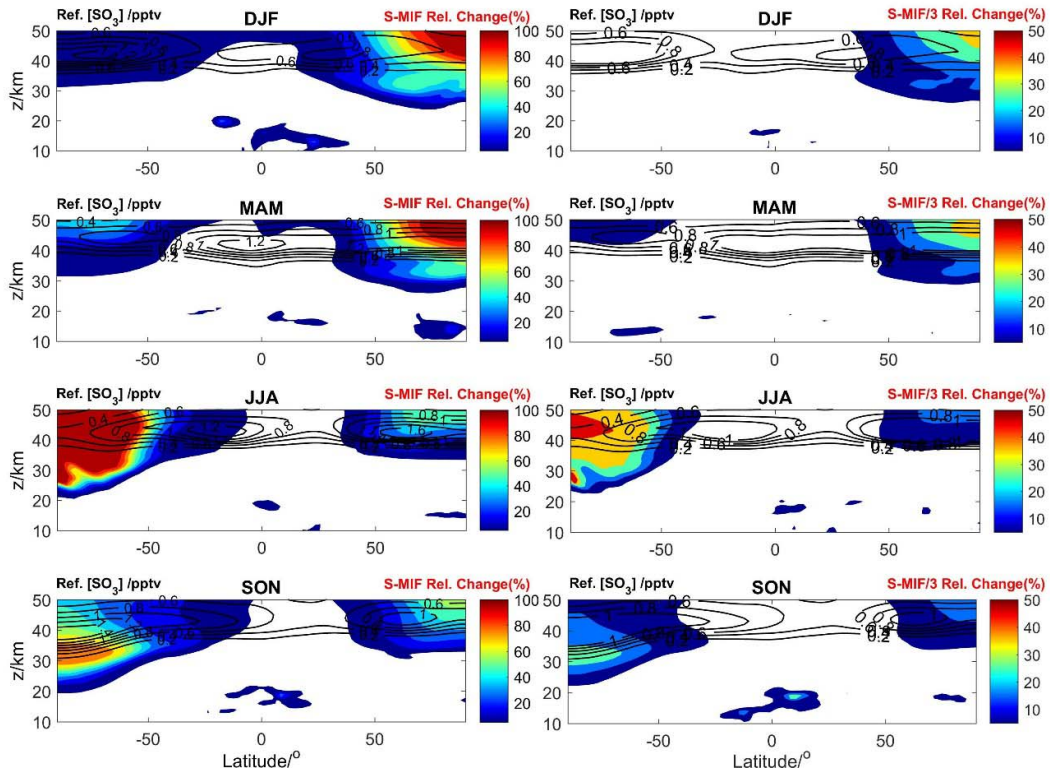

801

802 **Figure 6.** VMR seasonal averages vs. altitude and latitude of SO_3 in the stratosphere.
803 Contour lines: VMR for reference simulation. Filled color contours: percent change by
804 adding meteoric sulfur (left column: S-MIF simulation; right column: S MIF/3 simulation).

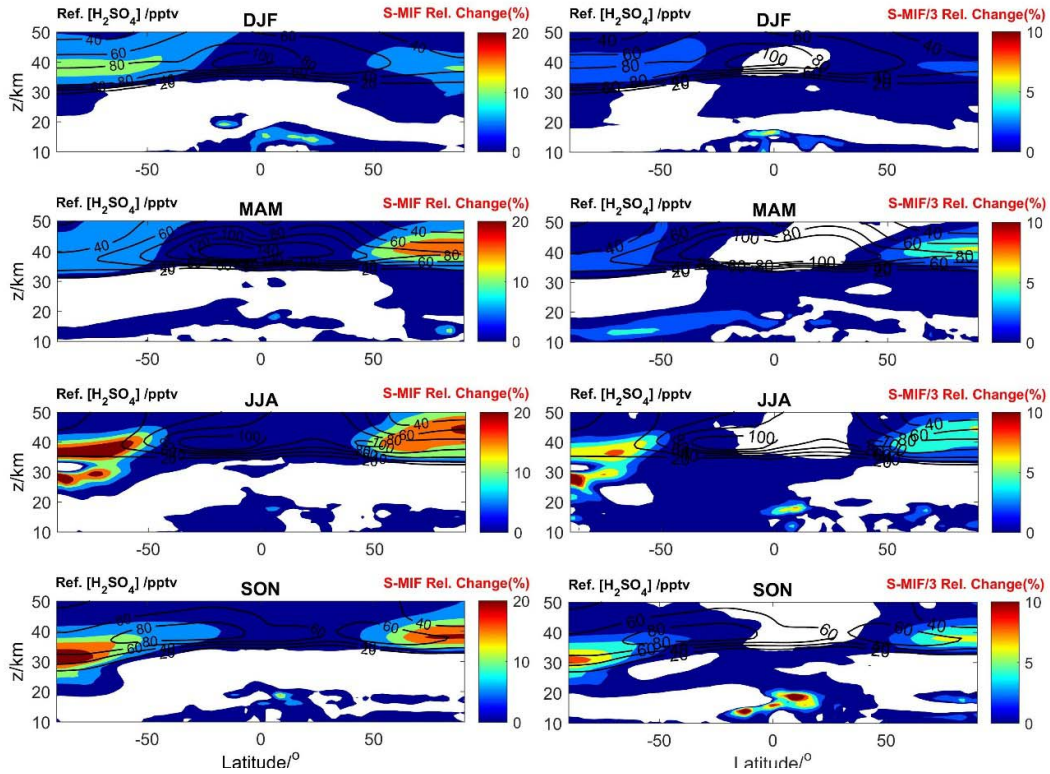

805

806 **Figure 7.** VMR seasonal averages vs. altitude and latitude of H_2SO_4 in the stratosphere.
807 Contour lines: VMR for reference simulation. Filled color contours: percent change by
808 adding meteoric sulfur (left column: S-MIF simulation; right column: S-MIF/3 simulation).

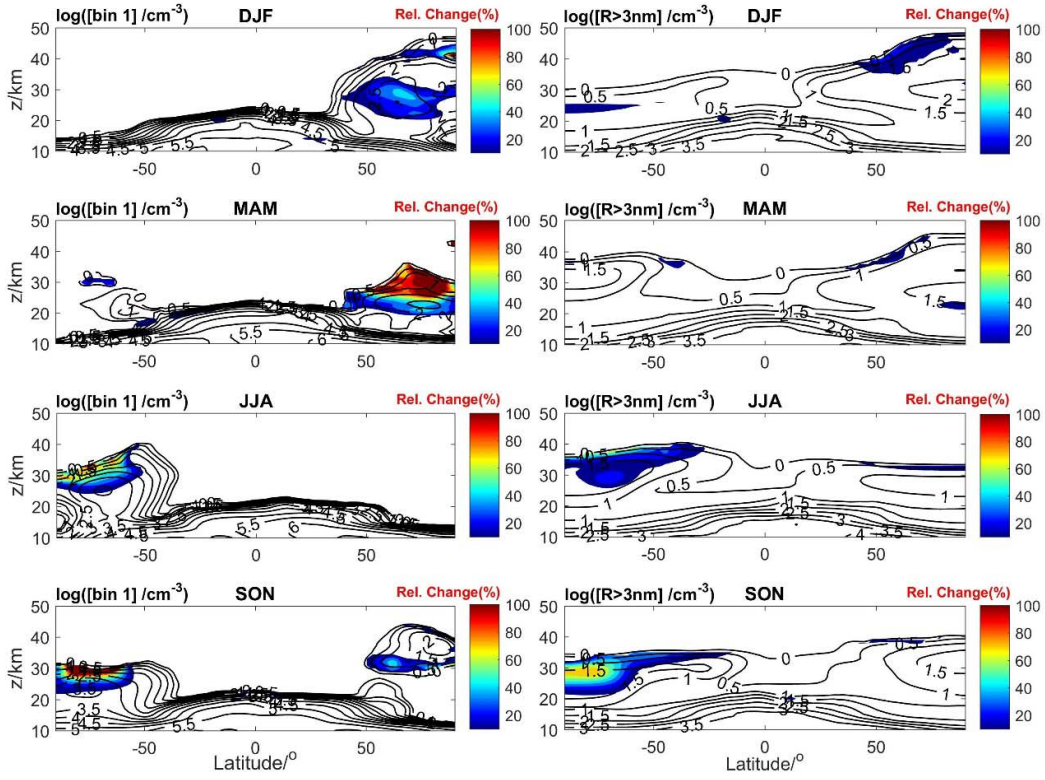

809

810 **Figure 8:** Number density seasonal averages vs altitude and latitude of pure sulfate
811 condensation nuclei. Left column: first size bin, right column: wet radius R > 3 nm. Black
812 contour lines: VMR for the model run without meteoric sulfur. Filled color contours: percent
813 change by adding meteoric sulfur (S-MIF simulation).

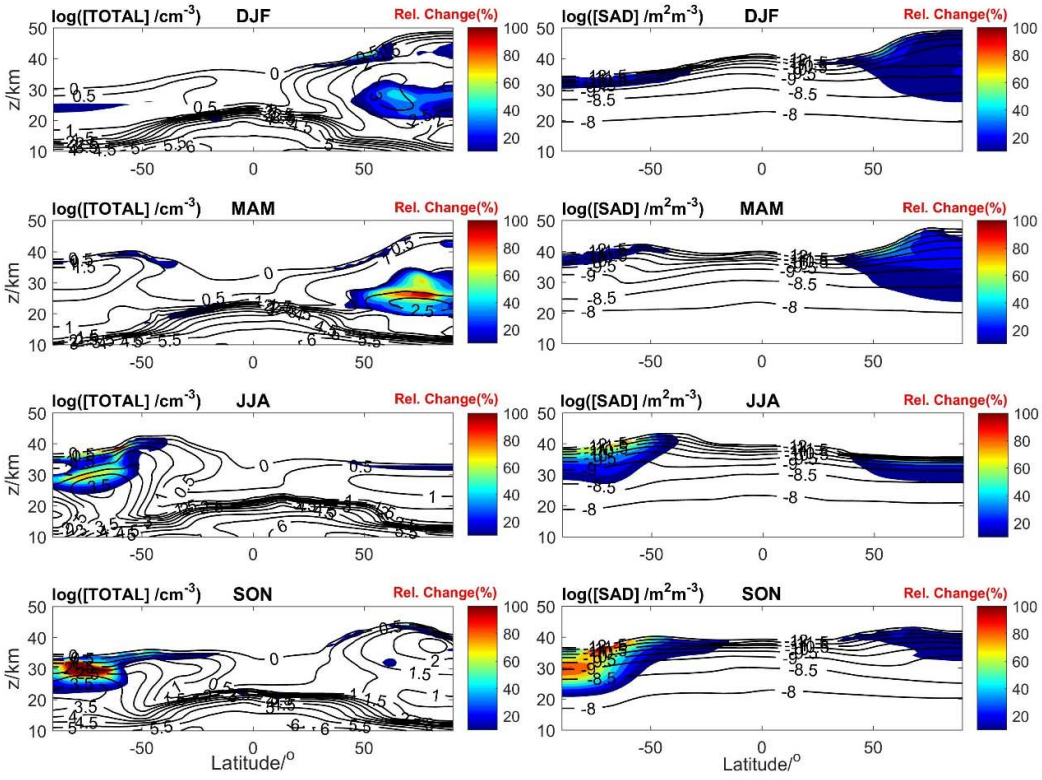

814

815 **Figure 9:** Number density seasonal averages vs altitude and latitude of the total number of
816 pure sulfate condensation nuclei (left column) and surface area density (SAD) (right
817 column). Black contour lines: VMR for the model run without meteoric sulfur. Filled color
818 contours: percent change by adding meteoric sulfur (S-MIF simulation).

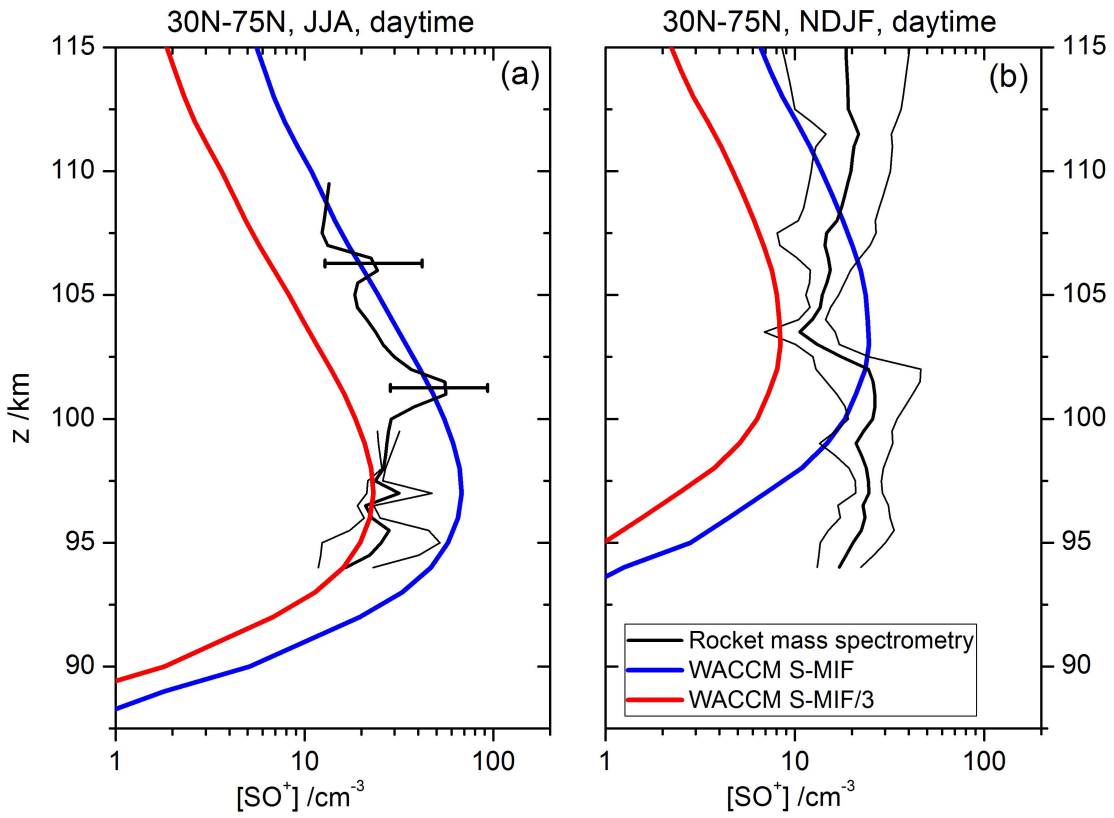

819

820 **Figure 10:** Observed (black) and modeled (S-MIF in blue and S-MIF/3 in red) vertical
821 profiles of SO^+. Panel *a*: Summer NH (average of S26/1, S26/2, SP37 and 18.10006, see text
822 for description of rocket flights). Only one measurement was available above 100 km. Panel
823 *b*: Fall-Winter NH (average of 18.10008, 33.009, 33.010, 18.020 and 18.021). Observations:
824 geometric mean and geometric standard deviation. Model: daytime zonal average (35-70N)
825 profiles for the corresponding months. The uncertainty of the observations is of the order of
826 100% [*Swider et al.*, 1979].

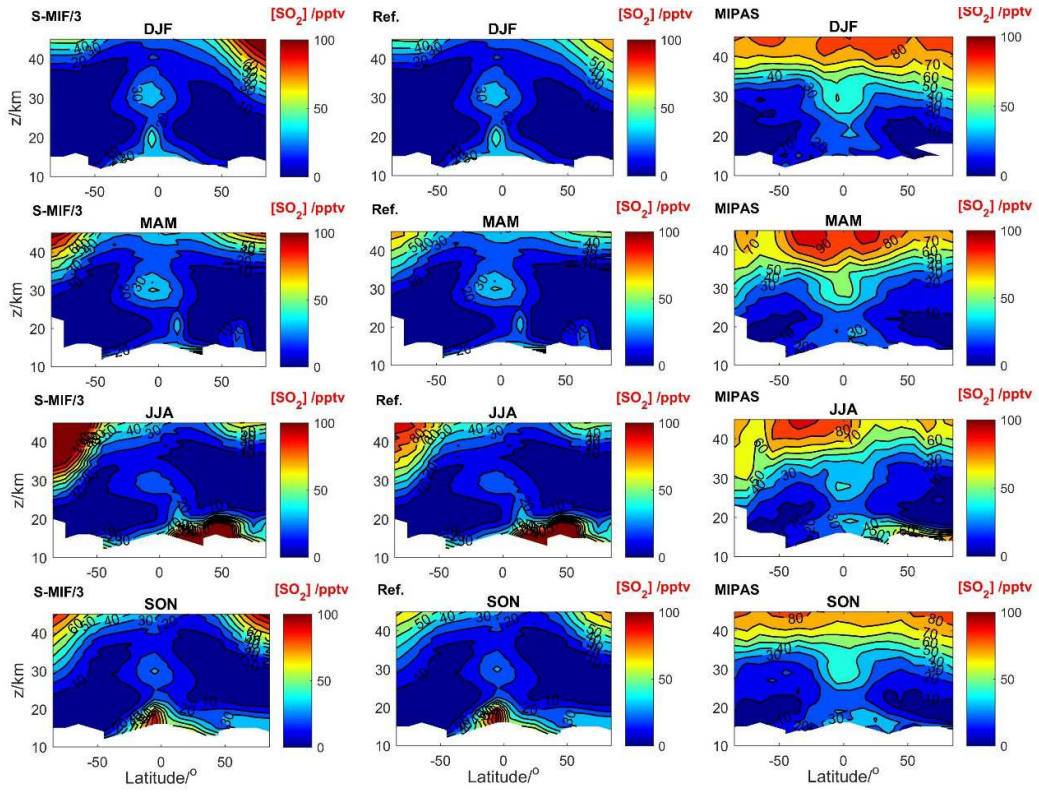

827

828 **Figure 11:** SO_2 VMR seasonal averages vs. altitude and latitude (2002-2012). Left column:
829 S-MIF/3 run. Middle column: reference run. Right column: MIPAS. The model results have
830 been smoothed vertically and latitudinally as indicated in the text.

831

832

833

834

835

836

837

838

839

840

841

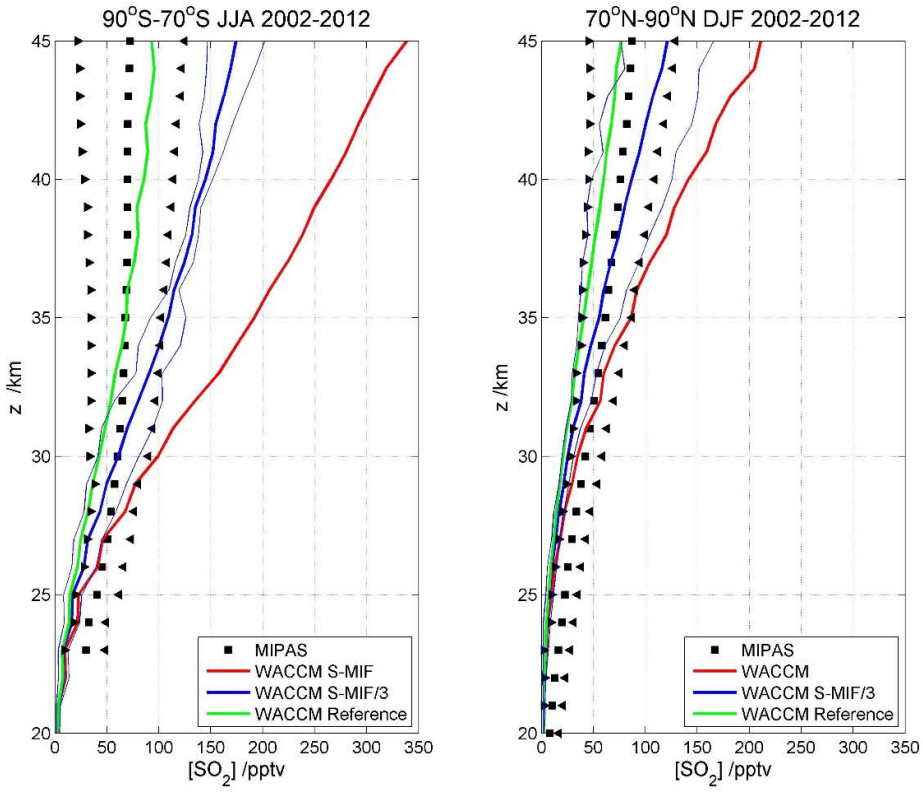

842

843 **Figure 12.** Zonal averages of SO_2 VMRs as a function of altitude, for the Polar Regions in
844 the winter hemisphere. MIPAS observations are shown by squares, and the reported
845 variability range (1 standard deviation) is given by triangles [*Höpfner et al.*, 2013]. The
846 reference, S-MIF and S-MIF/3 simulations are shown by green, red and blue thick lines,
847 respectively. The variability range within the winter season for the S-MIF/3 simulation is
848 given by blue thin lines. The reference run generally falls within the variability range of the
849 observations, while the S-MIF run overestimates by a factor of 3 and 5 for the Artic and the
850 Antarctic zones respectively. The S-MIF/3 run is broadly compatible with the observation,
851 since the variability range of the simulations generally overlaps with the observational range.

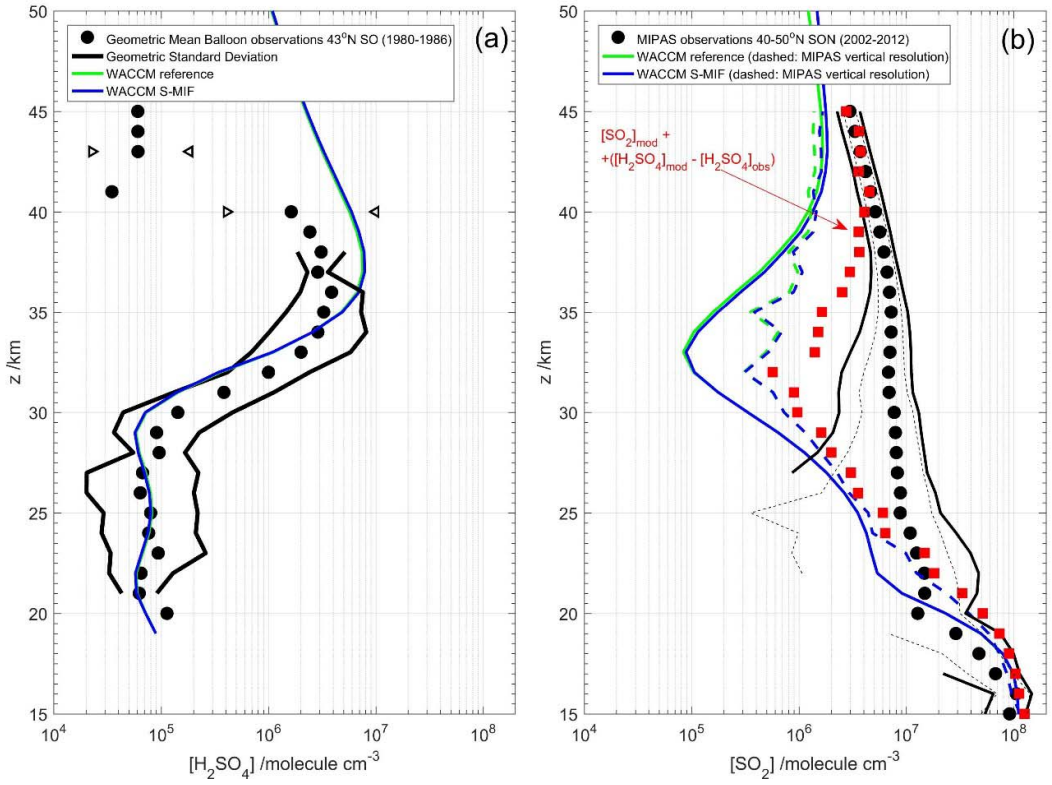

852

853 **Figure 13**: Panel *a*: geometric mean of balloon observations at 43º N (Laramie, USA) carried
854 out during September and October between 1980 and 1986. Modeled profiles from the
855 reference and S-MIF runs are shown as continuous lines. Panel *b*: comparison of the MIPAS
856 SO_2 number density vertical profile for 40º - 50º N and September-November 2002-2012 to
857 the corresponding modeled reference and S-MIF profiles. Thick black solid lines indicate the
858 variability of the observations (1 standard deviation) and the thin dashed lines the uncertainty
859 of the retrieval. Modeled profiles smoothed with the vertical resolution of the instrument as
860 indicated in the test are shown by dashed lines. The red squares show the result of adding to
861 the modeled, unsmoothed SO_2 vertical profile the difference between the observed and
862 modeled H_2SO_4 balloon vertical profiles in panel *a*, and then smoothing with the MIPAS
863 vertical resolution.

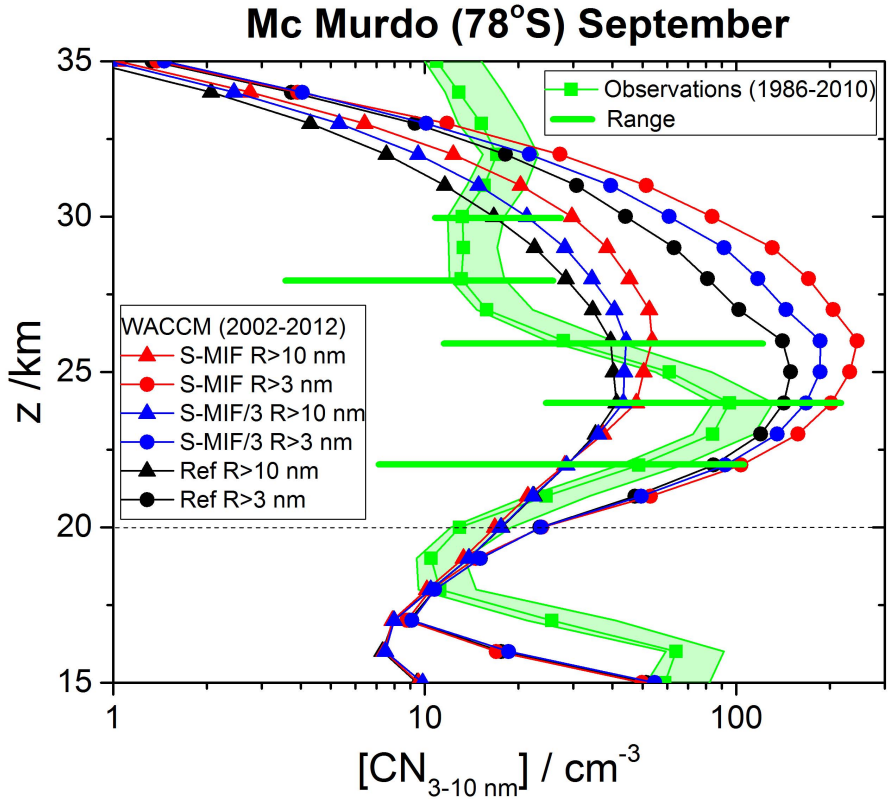

Figure 14: September monthly averages of CN balloon observations at McMurdo Antarctic research station (78º S) between 1986 and 2010 (squares). The shaded areas indicate the uncertainty of the measurements and the horizontal bars the variability range [*Campbell and Deshler*, 2014]. The cut-off radius of the observations is 3 nm below 50 hPa (~20 km, dotted horizontal line) and increases towards 10 nm for lower pressure (higher altitude). The corresponding monthly averages at the same location from the reference, the S-MIF/3 and the S-MIF model runs are shown in black, blue and red, respectively. Circles and triangles represent modeled CN with R > 3 nm and R > 10 nm, respectively.

875 **References**

876 Aikin, A. C., and R. A. Goldberg (1973), Metallic ions in the equatorial ionosphere, *J.*
877 *Geophys. Res.*, *78*(4), 734-745.

878 Anicich, V. G. (2003), An Index of the Literature for Bimolecular Gas Phase Cation-
879 Molecule Reaction Kinetics, JPL-NASA, Pasadena, California.

880 Arndt, P., J. Bohsung, M. Maetz, and E. K. Jessberger (1996), The elemental abundances in
881 interplanetary dust particles, *Meteorit. Planet. Sci.*, *31*(6), 817-833.

882 Bardeen, C. G., O. B. Toon, E. J. Jensen, D. R. Marsh, and V. L. Harvey (2008), Numerical
883 simulations of the three-dimensional distribution of meteoric dust in the mesosphere
884 and upper stratosphere, *J. Geophys. Res. [Atmos.]*, *113*(D17), D17202.

885 Ben Houria, A., Z. Ben Lakhdar, and M. Hochlaf (2006), Spectroscopic and spin-orbit
886 calculations on the SO^+ radical cation, *J. Chem. Phys.*, *124*(5), 054313.

887 Bones, D. L., J. C. Gómez Martín, C. J. Empson, J. D. Carrillo-Sánchez, A. D. James, T. P.
888 Conroy, and J. M. C. Plane (2016), A novel instrument to measure differential
889 ablation of meteorite samples and proxies: the Meteoric Ablation Simulator (MASI)
890 *Rev. Sci. Instrum.*, *87*, 094504.

891 Brownlee, D. E. (1996), The Elemental Composition of Interplanetary Dust, in *Physics,*
892 *Chemistry, and Dynamics of Interplanetary Dust, ASP Conference Series, 104*, edited
893 by B. A. S. Gustafson and M. S. Hanner, Astronomical Society of the Pacific, San
894 Francisco.

895 Brühl, C., J. Lelieveld, P. J. Crutzen, and H. Tost (2012), The role of carbonyl sulphide as a
896 source of stratospheric sulphate aerosol and its impact on climate, *Atmos. Chem.*
897 *Phys.*, *12*(3), 1239-1253.

898 Brühl, C., J. Lelieveld, H. Tost, M. Höpfner, and N. Glatthor (2015), Stratospheric sulfur and
899 its implications for radiative forcing simulated by the chemistry climate model
900 EMAC, *J. Geophys. Res. [Atmos.]*, *120*(5), 2103-2118.

901 Burgess, R., I. P. Wright, and C. T. Pillinger (1991), Determination of sulphur-bearing
902 components in C1 and C2 carbonaceous chondrites by stepped combustion,
903 *Meteoritics*, *26*(1), 55-64.

904 Campbell, P., and T. Deshler (2014), Condensation nuclei measurements in the midlatitude
905 (1982–2012) and Antarctic (1986–2010) stratosphere between 20 and 35 km, *J.*
906 *Geophys. Res. [Atmos.]*, *119*(1), 137-152.

907 Campbell, P., M. Mills, and T. Deshler (2014), The global extent of the mid stratospheric CN
908 layer: A three-dimensional modeling study, *J. Geophys. Res. [Atmos.]*, *119*(2), 1015-
909 1030.

910 Carrillo-Sánchez, J. D., D. Nesvorný, P. Pokorný, D. Janches, and J. M. C. Plane (2016),
911 Sources of cosmmic Dust in the Earth's Atmosphere, *Geophys. Res. Lett.*, *43*(11),
912 11979-11986.

913 Court, R. W., and M. A. Sephton (2011), The contribution of sulphur dioxide from ablating
914 micrometeorites to the atmospheres of Earth and Mars, *Geochim. Cosmochim. Acta*,
915 *75*(7), 1704-1717.

916 Court, R. W., and M. A. Sephton (2014), New estimates of the production of volatile gases
917 from ablating carbonaceous micrometeoroids at Earth and Mars during an E-belt-type
918 Late Heavy Bombardment, *Geochim. Cosmochim. Acta*, *145*, 175-205.

919 Cziczo, D. J., D. S. Thomson, and D. M. Murphy (2001), Ablation, Flux, and Atmospheric
920 Implications of Meteors Inferred from Stratospheric Aerosol, *Science*, *291*(5509),
921 1772.

922 Danielache, S. O., S. Tomoya, A. Kondorsky, I. Tokue, and S. Nanbu (2014), Nonadiabatic
923 calculations of ultraviolet absorption cross section of sulfur monoxide: Isotopic
924 effects on the photodissociation reaction, *J. Chem. Phys.*, *140*(4), 044319.

925 Davis, D. D., R. B. Klemm, and M. Pilling (1972), A flash photolysis–resonance fluorescence
926 kinetics study of ground-state sulfur atoms: I. Absolute rate parameters for reaction of
927 S(3P) with O2(3Σ), *Int. J. Chem. Kinet.*, *4*(4), 367-382.

928 Dhomse, S. S., et al. (2014), Aerosol microphysics simulations of the Mt.~Pinatubo eruption
929 with the UM-UKCA composition-climate model, *Atmos. Chem. Phys.*, *14*(20), 11221-
930 11246.

931 English, J. M., O. B. Toon, M. J. Mills, and F. Yu (2011), Microphysical simulations of new
932 particle formation in the upper troposphere and lower stratosphere, *Atmos. Chem.*
933 *Phys.*, *11*(17), 9303-9322.

934 Fehsenfeld, F. C., and E. E. Ferguson (1973), Atmospheric atomic sulfur ion reactions, *J.*
935 *Geophys. Res.*, *78*(10), 1699-1701.

936 Feierabend, K. J., D. K. Havey, S. S. Brown, and V. Vaida (2006), Experimental absolute
937 intensities of the $4\nu_9$ and $5\nu_9$ O–H stretching overtones of H_2SO_4, *Chem. Phys. Lett.*,
938 *420*(4–6), 438-442.

939 Feng, W., D. R. Marsh, M. P. Chipperfield, D. Janches, J. Höffner, F. Yi, and J. M. C. Plane
940 (2013), A global atmospheric model of meteoric iron, *J. Geophys. Res. [Atmos.]*,
941 *118*(16), 9456-9474.

942 Fleming, E. L., S. Chandra, J. J. Barnett, and M. Corney (1990), Zonal mean temperature,
943 pressure, zonal wind and geopotential height as functions of latitude, *Adv. Space Res.*,
944 *10*(12), 11-59.

945 Florescu-Mitchell, A. I., and J. B. A. Mitchell (2006), Dissociative recombination, *Phys.*
946 *Rep.*, *430*(5–6), 277-374.

947 Frisch, M. J., et al. (2009), Gaussian 09, edited, Gaussian, Inc., Wallingford, CT, USA.

948 Gabrielli, P., et al. (2004), Meteoric smoke fallout over the Holocene epoch revealed by
949 iridium and platinum in Greenland ice, *Nature*, *432*(7020), 1011-1014.

950 Garcia, R. R., D. R. Marsh, D. E. Kinnison, B. A. Boville, and F. Sassi (2007), Simulation of
951 secular trends in the middle atmosphere, 1950–2003, *J. Geophys. Res. [Atmos.]*,
952 *112*(D9), D09301.

953 Garcia, R. R., M. López-Puertas, B. Funke, D. R. Marsh, D. E. Kinnison, A. K. Smith, and F.
954 González-Galindo (2014), On the distribution of CO2 and CO in the mesosphere and
955 lower thermosphere, *J. Geophys. Res. [Atmos.]*, *119*(9), 5700-5718.

956 Gardner, C. S., A. Z. Liu, and Y. Guo (2016), Vertical and horizontal transport of
957 mesospheric Na: Implications for the mass influx of cosmic dust, *J. Atmos. Sol. Terr.*
958 *Phys.*

959 Gardner, C. S., A. Z. Liu, D. R. Marsh, W. Feng, and J. M. C. Plane (2014), Inferring the
960 global cosmic dust influx to the Earth's atmosphere from lidar observations of the
961 vertical flux of mesospheric Na, *J. Geophys. Res. [Space Phys]*, *119*(9), 7870-7879.

962 Genge, M. J., M. M. Grady, and R. Hutchison (1997), The textures and compositions of fine-
963 grained Antarctic micrometeorites: Implications for comparisons with meteorites,
964 *Geochim. Cosmochim. Acta*, *61*(23), 5149-5162.

965 Georgievskii, Y., and S. J. Klippenstein (2005), Long-Range Transition State Theory, *J.*
966 *Chem. Phys.*, *122*(19), 194103.

967 Gómez Martín, J. C., and J. M. C. Plane (2011), Kinetic studies of atmospherically relevant
968 silicon chemistry. Part III: Reactions of Si^+ and SiO^+ with O_3, and Si^+ with O_2, *Phys.*
969 *Chem. Chem. Phys.*, *13*(9), 3764-3774.

970 Gómez Martín, J. C., D. L. Bones, J. D. Carrillo-Sánchez, A. D. James, J. M. Trigo-
971 Rodriguez, B. Fegley Jr., and J. M. C. Plane (2017), Novel Experimental Simulations
972 of the Atmospheric Injection of Meteoric Metals, *Astrophys. J.*, *836*(2), 212-237.

973 Greshake, A., A. Bischoff, and P. Hoppe (1996), Mineralogy, chemistry, and oxygen isotopes
974 of refractory inclusions from stratospheric interplanetary dust particles and
975 micrometeorites, *Meteorit. Planet. Sci.*, *31*(6), 739-748.

976 Greshake, A., W. KlÖCk, P. Arndt, M. Maetz, G. J. Flynn, S. Bajt, and A. Bischoff (1998),
977 Heating experiments simulating atmospheric entry heating of micrometeorites: Clues
978 to their parent body sources, *Meteorit. Planet. Sci.*, *33*(2), 267-290.

979 Herrmann, U., P. Eberhardt, M. A. Hidalgo, E. Kopp, and L. G. Smith (1978), Metal ions and
980 isotopes in sporatic E-layers during the Perseid meteor shower, in *Space Research*,
981 edited by M. J. Rycroft, pp. 249-252, Pergamon.

982 Hervig, M. E., C. G. Bardeen, D. E. Siskind, M. J. Mills, and R. Stockwell (2017), Meteoric
983 smoke and H2SO4 aerosols in the upper stratosphere and mesosphere, *Geophys. Res.*
984 *Lett.*, *44*(2), 1150-1157.

985 Hervig, M. E., L. L. Gordley, L. E. Deaver, D. E. Siskind, M. H. Stevens, J. M. Russell, S.
986 M. Bailey, L. Megner, and C. G. Bardeen (2009), First Satellite Observations of
987 Meteoric Smoke in the Middle Atmosphere, *Geophys. Res. Lett.*, *36*(18), L18805.

988 Höpfner, M., et al. (2013), Sulfur dioxide (SO_2) as observed by MIPAS/Envisat: temporal
989 development and spatial distribution at 15–45 km altitude, *Atmos. Chem. Phys.*,
990 *13*(20), 10405-10423.

991 Höpfner, M., et al. (2015), Sulfur dioxide (SO_2) from MIPAS in the upper troposphere and
992 lower stratosphere 2002–2012, *Atmos. Chem. Phys.*, *15*(12), 7017-7037.

993 Huang, W., X. Chu, C. S. Gardner, J. D. Carrillo-Sánchez, W. Feng, J. M. C. Plane, and D.
994 Nesvorný (2015), Measurements of the vertical fluxes of atomic Fe and Na at the
995 mesopause: Implications for the velocity of cosmic dust entering the atmosphere,
996 *Geophys. Res. Lett.*, *42*(1), 169-175.

997 Hutchison, R. (2004), *Meteorites*, Cambridge University Press, Cambridge, UK.

998 Istomin, V. G. (1963), Ions of extra-terrestrial origin in the earth's ionosphere, *Plan. Space*
999 *Sci.*, *11*(2), 173-174.

1000 Jessberger, E., T. Stephan, D. Rost, P. Arndt, M. Maetz, F. Stadermann, D. Brownlee, J.
1001 Bradley, and G. Kurat (2001), Properties of Interplanetary Dust: Information from
1002 Collected Samples, in *Interplanetary Dust*, edited by E. Grün, B. S. Gustafson, S.
1003 Dermott and H. Fechtig, pp. 253-294, Springer Berlin Heidelberg.

1004 Jurewicz, A. J. G., D. W. Mittlefehldt, and J. H. Jones (1993), Experimental partial melting of
1005 the Allende (CV) and Murchison (CM) chondrites and the origin of asteroidal basalts,
1006 *Geochim. Cosmochim. Acta*, *57*(9), 2123-2139.

1007 Kim, S. J., and M. F. A'Hearn (1991), Upper limits of SO and SO_2 in Comets, *Icarus*, *90*(1),
1008 79-95.

1009 Klöck, W., G. J. Flynn, S. R. Sutton, S. Bajt, and K. Neuking (1994), Heating Experiments
1010 Simulating Atmospheric Entry of Micrometeorites, paper presented at 25th Lunar and
1011 Planetary Science Conference, Houston, USA.

1012 Kopp, E. (1997), On the abundance of metal ions in the lower ionosphere, *J. Geophys. Res.*
1013 *[Space Phys]*, *102*(A5), 9667-9674.

1014 Kopp, E., H. Ramseyer, and L. G. Björn (1984), Positive ion composition and electron
1015 density in a combined auroral and NLC event, *Adv. Space Res.*, *4*(4), 157-161.

1016 Kopp, E., L. André, and L. G. Smith (1985a), Positive ion composition and derived particle
1017 heating in the lower auroral ionosphere, *J. Atmos. Terr. Phys.*, *47*(1), 301-308.

1018 Kopp, E., P. Eberhardt, U. Herrmann, and L. G. Björn (1985b), Positive ion composition of
1019 the high-latitude summer D region with noctilucent clouds, *J. Geophys. Res. [Atmos.]*,
1020 *90*(D7), 13041-13053.

1021 Kovács, T., et al. (2017), Determination of the atmospheric lifetime and global warming
1022 potential of sulfur hexafluoride using a three-dimensional model, *Atmos. Chem. Phys.*,
1023 *17*(2), 883-898.

1024 Kring, D. A., H. J. Melosh, and D. M. Hunten (1996), Impact-induced perturbations of
1025 atmospheric sulfur, *Earth. Planet. Sci. Lett.*, *140*(1–4), 201-212.

Kurat, G., C. Koeberl, T. Presper, F. Brandstätter, and M. Maurette (1994), Petrology and geochemistry of Antarctic micrometeorites, *Geochim. Cosmochim. Acta*, *58*(18), 3879-3904.

Lamarque, J. F., et al. (2012), CAM-chem: description and evaluation of interactive atmospheric chemistry in the Community Earth System Model, *Geosci. Model Dev.*, *5*(2), 369-411.

Lamarque, J. F., et al. (2010), Historical (1850–2000) gridded anthropogenic and biomass burning emissions of reactive gases and aerosols: methodology and application, *Atmos. Chem. Phys.*, *10*(15), 7017-7039.

Lane, J. R., and H. G. Kjaergaard (2008), Calculated Electronic Transitions in Sulfuric Acid and Implications for Its Photodissociation in the Atmosphere, *J. Phys. Chem. A*, *112*(22), 4958-4964.

Langowski, M. P., C. von Savigny, J. P. Burrows, W. Feng, J. M. C. Plane, D. R. Marsh, D. Janches, M. Sinnhuber, A. C. Aikin, and P. Liebing (2015), Global investigation of the Mg atom and ion layers using SCIAMACHY/Envisat observations between 70 and 150 km altitude and WACCM-Mg model results, *Atmos. Chem. Phys.*, *15*(1), 273-295.

Linstrom, P. J. E. (2016), NIST Chemistry WebBook (NIST Standard Reference Database Number 69), edited, NIST.

Love, S. G., and D. E. Brownlee (1991), Heating and thermal transformation of micrometeoroids entering the Earth's atmosphere, *Icarus*, *89*(1), 26-43.

Marsh, D. R., D. Janches, W. Feng, and J. M. C. Plane (2013a), A global model of meteoric sodium, *J. Geophys. Res. [Atmos.]*, *118*(19), 11,442-411,452.

Marsh, D. R., M. J. Mills, D. E. Kinnison, J.-F. Lamarque, N. Calvo, and L. M. Polvani (2013b), Climate Change from 1850 to 2005 Simulated in CESM1(WACCM), *J. Clim.*, *26*(19), 7372-7391.

Marsh, D. R., R. R. Garcia, D. E. Kinnison, B. A. Boville, F. Sassi, S. C. Solomon, and K. Matthes (2007), Modeling the whole atmosphere response to solar cycle changes in radiative and geomagnetic forcing, *J. Geophys. Res. [Atmos.]*, *112*(D23), D23306.

Megner, L., D. E. Siskind, M. Rapp, and J. Gumbel (2008), Global and temporal distribution of meteoric smoke: A two-dimensional simulation study, *J. Geophys. Res. [Atmos.]*, *113*(D3), D03202.

Meister, J., P. Eberhardt, U. Herrmann, E. Kopp, M. A. Hidalgo, and J. Sechrist, CF. (1978), D-region ion composition during the winter anomaly campaign on January 8, 1977., *Space Res. XVIII*, 155-159.

Miller, Y., R. B. Gerber, and V. Vaida (2007), Photodissociation yields for vibrationally excited states of sulfuric acid under atmospheric conditions, *Geophys. Res. Lett.*, *34*(16), L16820.

1064 Mills, M. J., O. B. Toon, and G. E. Thomas (2005a), Mesospheric sulfate aerosol layer, *J.*
1065 *Geophys. Res. [Atmos.]*, *110*(D24), D24208.

1066 Mills, M. J., O. B. Toon, V. Vaida, P. E. Hintze, H. G. Kjaergaard, D. P. Schofield, and T. W.
1067 Robinson (2005b), Photolysis of sulfuric acid vapor by visible light as a source of the
1068 polar stratospheric CN layer, *J. Geophys. Res. [Atmos.]*, *110*(D8), D08201.

1069 Mills, M. J., et al. (2016), Global volcanic aerosol properties derived from emissions, 1990–
1070 2014, using CESM1(WACCM), *J. Geophys. Res. [Atmos.]*, *121*(5), 2332-2348.

1071 Murphy, D. M., D. S. Thomson, and M. J. Mahoney (1998), In Situ Measurements of
1072 Organics, Meteoritic Material, Mercury, and Other Elements in Aerosols at 5 to 19
1073 Kilometers, *Science*, *282*(5394), 1664-1669.

1074 Murphy, D. M., K. D. Froyd, J. P. Schwarz, and J. C. Wilson (2014), Observations of the
1075 chemical composition of stratospheric aerosol particles, *Q. J. Roy. Meteorol. Soc.*,
1076 *140*(681), 1269-1278.

1077 Narcisi, R. S. (1969), On water cluster ions in the ionospheric D-region, in *Planetary*
1078 *Electrodynamics*, edited by S. C. Coroniti and J. Hughes, p. 447, Gordon and Breach,
1079 New York.

1080 Narcisi, R. S., and A. D. Bailey (1965), Mass spectrometric measurements of positive ions at
1081 altitudes from 64 to 112 kilometers, *J. Geophys. Res.*, *70*(15), 3687-3700.

1082 Neely, R. R., J. M. English, O. B. Toon, S. Solomon, M. Mills, and J. P. Thayer (2011),
1083 Implications of extinction due to meteoritic smoke in the upper stratosphere, *Geophys.*
1084 *Res. Lett.*, *38*(24), L24808.

1085 Newhall, C. G., and S. Self (1982), The volcanic explosivity index (VEI) an estimate of
1086 explosive magnitude for historical volcanism, *J. Geophys. Res. [Oceans]*, *87*(C2),
1087 1231-1238.

1088 Ogawa, T., and T. Shimazaki (1975), Diurnal variations of odd nitrogen and ionic densities in
1089 the mesosphere and lower thermosphere: Simultaneous solution of photochemical-
1090 diffusive equations, *J. Geophys. Res.*, *80*(28), 3945-3960.

1091 Parthiban, S., and J. M. L. Martin (2001), Assessment of W1 and W2 theories for the
1092 computation of electron affinities, ionization potentials, heats of formation, and
1093 proton affinities, *J. Chem. Phys.*, *114*(14), 6014-6029.

1094 Phillips, L. F. (1981), Absolute absorption cross sections for SO between 190 and 235 nm, *J.*
1095 *Phys. Chem.*, *85*(26), 3994-4000.

1096 Plane, J. M. C. (2012), Cosmic dust in the Earth's atmosphere, *Chem. Soc. Rev.*, *41*(19),
1097 6507-6518.

1098 Plane, J. M. C., W. Feng, and E. C. M. Dawkins (2015), The Mesosphere and Metals:
1099 Chemistry and Changes, *Chem. Rev.*, *115*(10), 4497-4541.

1100 Plane, J. M. C., J. C. Gomez Martin, W. Feng, and D. Janches (2016), Silicon chemistry in
1101 the mesosphere and lower thermosphere, *J. Geophys. Res. [Atmos.]*, *121*(7), 3718-
1102 3728.

1103 Richter, J. H., F. Sassi, and R. R. Garcia (2010), Toward a Physically Based Gravity Wave
1104 Source Parameterization in a General Circulation Model, *J. Atmos. Sci.*, *67*(1), 136-
1105 156.

1106 Rienecker, M. M., et al. (2011), MERRA: NASA's Modern-Era Retrospective Analysis for
1107 Research and Applications, *J. Climate*, *24*(14), 3624-3648.

1108 Rienecker, M. M., et al. (2011), MERRA: NASA's Modern-Era Retrospective Analysis for
1109 Research and Applications, *J. Clim.*, *24*(14), 3624-3648.

1110 Rinsland, C. P., M. R. Gunson, M. K. W. Ko, D. W. Weisenstein, R. Zander, M. C. Abrams,
1111 A. Goldman, N. D. Sze, and G. K. Yue (1995), H2SO4 photolysis: A source of sulfur
1112 dioxide in the upper stratosphere, *Geophys. Res. Lett.*, *22*(9), 1109-1112.

1113 Rollins, A. W., et al. (2017), The role of sulfur dioxide in stratospheric aerosol formation
1114 evaluated by using in situ measurements in the tropical lower stratosphere, *Geophys.*
1115 *Res. Lett.*, *44*(9), 4280-4286.

1116 Sander, S. P., et al. (2011), Chemical Kinetics and Photochemical Data for Use in
1117 Atmospheric Studies, Evaluation No. 17, JPL Publication 10-6, Jet Propulsion
1118 Laboratory, Pasadena, http://jpldataeval.jpl.nasa.gov.

1119 Saunders, R. W., S. Dhomse, W. S. Tian, M. P. Chipperfield, and J. M. C. Plane (2012),
1120 Interactions of meteoric smoke particles with sulphuric acid in the Earth's
1121 stratosphere, *Atmos. Chem. Phys.*, *12*(10), 4387-4398.

1122 Scharringhausen, M., A. C. Aikin, J. P. Burrows, and M. Sinnhuber (2008), Global column
1123 density retrievals of mesospheric and thermospheric Mg I and Mg II from
1124 SCIAMACHY limb and nadir radiance data, *J. Geophys. Res. [Atmos.]*, *113*(D13),
1125 D13303.

1126 Schramm, L. S., D. E. Brownlee, and M. M. Wheelock (1989), Major element composition of
1127 stratospheric micrometeorites, *Meteoritics*, *24*(2), 99-112.

1128 Schulz, R., et al. (2015), Comet 67P/Churyumov-Gerasimenko sheds dust coat accumulated
1129 over the past four years, *Nature*, *518*, 216–218.

1130 Smith, A. K. (2012), Global Dynamics of the MLT, *Surv. Geophys.*, *33*(6), 1177-1230.

1131 Smith, A. K., R. R. Garcia, D. R. Marsh, and J. H. Richter (2011), WACCM simulations of
1132 the mean circulation and trace species transport in the winter mesosphere, *J. Geophys.*
1133 *Res. [Atmos.]*, *116*(D20), D20115.

1134 Smith, S. J., J. van Aardenne, Z. Klimont, R. J. Andres, A. Volke, and S. Delgado Arias
1135 (2011), Anthropogenic sulfur dioxide emissions: 1850–2005, *Atmos. Chem. Phys.*,
1136 *11*(3), 1101-1116.

1137 SPARC (2006), SPARC Assessment of Stratospheric Aerosol Properties (ASAP), SPARC
1138 Report, SPARC Office.

1139 Swider, W. (1969), Processes for meteoric elements in the E-region, *Plan. Space Sci.*, *17*(6),
1140 1233-1246.

1141 Swider, W., E. Murad, and U. Herrmann (1979), Sulfur chemistry in the E-region, *Geophys.*
1142 *Res. Lett.*, *6*(7), 560-562.

1143 Swinbank, R., and D. A. Ortland (2003), Compilation of wind data for the Upper Atmosphere
1144 Research Satellite (UARS) Reference Atmosphere Project, *J. Geophys. Res. [Atmos.]*,
1145 *108*(D19), 4615.

1146 Taylor, S., G. Matrajt, and Y. Guan (2012), Fine-grained precursors dominate the
1147 micrometeorite flux, *Meteorit. Planet. Sci.*, *47*(4), 550-564.

1148 Taylor, S., K. W. Jones, G. F. Herzog, and C. E. Hornig (2011), Tomography: A window on
1149 the role of sulfur in the structure of micrometeorites, *Meteorit. Planet. Sci.*, *46*(10),
1150 1498-1509.

1151 Thomas, K. L., L. P. Keller, and D. S. McKay (1996), A Comprehensive Study of Major,
1152 Minor, and Light Element Abundances in over 100 Interplanetary Dust Particles, in
1153 *Physics, Chemistry, and Dynamics of Interplanetary Dust, ASP Conference Series,*
1154 *104*, edited by B. A. S. Gustafson and M. S. Hanner, Astronomical Society of the
1155 Pacific, San Francisco.

1156 Toon, O. B., R. P. Turco, D. Westphal, R. Malone, and M. Liu (1988), A Multidimensional
1157 Model for Aerosols: Description of Computational Analogs, *J. Atmos. Sci.*, *45*(15),
1158 2123-2144.

1159 Toppani, A., G. Libourel, C. Engrand, and M. Maurette (2001), Experimental simulation of
1160 atmospheric entry of micrometeorites, *Meteorit. Planet. Sci.*, *36*(10), 1377-1396.

1161 Trigo-Rodriguez, J. M., and J. Llorca (2007), On the sodium overabundance in cometary
1162 meteoroids, *Adv. Space Res.*, *39*(4), 517-525.

1163 Turco, R. P., O. B. Toon, P. Hamill, and R. C. Whitten (1981), Effects of meteoric debris on
1164 stratospheric aerosols and gases, *J. Geophys. Res. [Oceans]*, *86*(C2), 1113-1128.

1165 Vaida, V., H. G. Kjaergaard, P. E. Hintze, and D. J. Donaldson (2003), Photolysis of Sulfuric
1166 Acid Vapor by Visible Solar Radiation, *Science*, *299*(5612), 1566.

1167 Vondrak, T., J. M. C. Plane, S. Broadley, and D. Janches (2008), A chemical model of
1168 meteoric ablation, *Atmos. Chem. Phys.*, *8*(23), 7015-7031.

1169 Wallis, M. K., and K. S. K. Swamy (1988), Some diatomic molecules from comet P/Halley's
1170 UV spectra near spacecraft flybys, in *Exploration of Halley's Comet*, edited by M.
1171 Grewing, F. Praderie and R. Reinhard, pp. 329-332, Springer Berlin Heidelberg,
1172 Berlin, Heidelberg.

1173 Whyte, A. R., and L. F. Phillips (1982), Sulfur monoxide (B-X) bands. Tests of the effects of
1174 sulfur monoxide decay and energy transfer from molecular oxygen($^1\Delta_g$) on measured

sulfur monoxide absorption cross sections in the atomic oxygen + carbon disulfide reaction system, *J. Phys. Chem.*, *86*(22), 4327-4330.

Zbinden, P. A., M. A. Hidalgo, P. Eberhahdt, and J. Geiss (1975), Mass spectrometer measurements of the positive ion composition in the D- and E-regions of the ionosphere, *Plan. Space Sci.*, *23*(12), 1621-1642.